Self-organization and emergence of memory in a cyclically driven elastoplastic model of an amorphous solid

Dheeraj Kumar [1,*] Muhittin Mungan [2] Sylvain Patinet [1] M. Mert Terzi [1] and Damien Vandembroucq [1,†]
[1] *PMMH, CNRS, ESPCI Paris, Université PSL, Sorbonne Université, Université Paris Cité, France*
[2] *Institute for Biological Physics, University of Cologne, Zülpicher Straße 77, Cologne, Germany*

(Received 11 April 2025; accepted 4 August 2025; published 15 September 2025)

The mechanical behavior of disordered materials, such as dense suspensions, glasses, and granular materials, depends on their thermal and mechanical history. Under periodic driving, these materials can evolve into states that encode a memory of their annealing. Such memory effects have been observed experimentally in systems ranging from sheared non-Brownian suspensions to crumpled elastic sheets and in atomistic simulations. Here, we show that a quenched mesoscopic elastoplastic model of a sheared amorphous solid reproduces the phenomena of self-organization and memory formation under mechanical annealing. We analyze sample-to-sample fluctuations under readout protocols and demonstrate their connection to the irreversibility transition. Our model allows us to understand in detail the mechanical processes underlying memory formation. We find that annealing by cyclic shear leads to the self-organization of plasticity, which can be characterized by a density of local mechanical stress thresholds. These thresholds exhibit anisotropy, depending on their alignment with the driving direction. The interplay between these thresholds dictates how the driving history—particularly its direction and amplitude—is imprinted into the material's local structure. We develop readout protocols capable of accessing both the amplitude and the direction of the mechanical training. Our findings can be understood within the framework of return point memory which emerges as a result of mechanical annealing. Building on this, we develop a Preisach-like model of directional memory that describes well our numerical results. We conclude with a discussion of similarities of the evolution of plasticity under mechanical annealing and adaptive evolution in changing environments.

DOI: 10.1103/nytl-pnfm

I. INTRODUCTION

From toothpaste and polymers to glass and concrete, most everyday materials are disordered: they do not have a regular atomic or particle-scale structure. Unlike crystalline materials, for which there is a single, well-defined thermodynamic state, disordered materials are out of equilibrium and can be found in a myriad of different states. Not all these states are equivalent, so the physical and mechanical properties of disordered solids or complex fluids usually depend on how they are prepared and processed. In other words, most of these materials have a partial memory of their thermal and mechanical past.

However, what exactly is the nature of this memory? What information can be recorded and subsequently read out in a disordered material? How is it connected to the underlying structure of the material? Over the past decade, the characterization and understanding of mechanical memory in materials has motivated a growing number of studies [1–5]. In particular, experimental works on colloidal suspensions [6–12], as well as particle simulations of disordered solids upon oscillatory driving [13–15], demonstrated the existence of a dynamic transition, the irreversibility transition, connecting a reversible state at low amplitude, in which the same sequence of plastic events repeats periodically with a diffusive state at high amplitude [13,14,16,17]. In a parallel line of research, experimental and numerical studies explored the limit cycles reached after oscillatory driving to understand in more detail the memory capacity of disordered solids [12,18–26]. This research demonstrated that, when combined with a properly defined readout protocol, it is possible to record and subsequently retrieve the amplitude of oscillatory shear that had been applied beforehand, i.e., during "training," to the material.

At the heart of these memory phenomena is the emergence of a high degree of reversibility by mechanical annealing through cyclic shear. As a result, deformation protocols allow the system to return to the vicinity of previously visited states. Such a behavior is reminiscent of nested hysteresis cycles in magnets, where it is attributed to return-point memory (RPM) [27–30]. RPM describes a particular form of nesting in which hysteresis cycles return to their parent cycles at the point where they initially entered the subcycle. However, unlike magnetic spin systems, plastic events in disordered materials are coupled through an elastic, long-range, anisotropic interaction. Not only can such interactions destabilize other regions of the sample, but they can also stabilize them. This property renders such systems different from ferromagnets, where the effect of interactions is always destabilizing and can be rigorously shown to lead to RPM [30–32]. In disordered systems, where the effect of interactions can go both ways,

*Contact author: dheeraj.kumar@espci.fr
†Contact author: damien.vandembroucq@espci.fr

this sufficient condition is no longer satisfied and one would, therefore, not expect RPM to emerge a priori. Nevertheless, approximate RPM with a hierarchy of nested hysteresis cycle has been observed in such systems—both experimentally and numerically [12,33].

The hysteresis observed in athermal-driven disordered systems is due to local instabilities, such as the buckling of creases of a crumpled thin elastic sheet [3,34] or the local plastic rearrangements of the amorphous structure for glasses [35,36]. Following the spirit of the Preisach model that was initially developed to describe hysteresis in magnets [27–29,37,38], mechanical memory has often been modelled as a collection of *hysterons*, i.e., elementary units of hysteresis [12,39–45]. Models of collections of interacting hysterons have been successfully used to explain features of the cyclic response, such as the memory of amplitude and direction, as well as multiperiodic responses, i.e., cyclic response whose period is a multiple of the period of driving [46–48]. In essence, the disordered landscape of such models is fixed once and for all and hence does not co-evolve with the mechanical annealing. In other words, these models take the mechanically annealed state as given, modeling it as a system of hysterons with some fixed and prescribed interactions. However, experiments and simulations of driven disordered systems show that mechanical reversibility and memory formation is an *emergent* phenomenon. It is a consequence of the mechanical annealing, which causes the properties of the system and its response to gradually change [15,19,49–51]. Thus, models of collections of interacting hysterons, as considered for example in Refs. [46–48], while capable of characterizing the response of the annealed system, are unable to cope with the complex processes of self-organization that lead to mechanical memory in driven disordered materials.

To overcome these limitations, an appealing alternative is to resort to mesoscopic elastoplastic models [52]. These lattice models rely on local threshold dynamics in which each cell can experience a local slip whenever the local stress reaches a prescribed threshold value. Each cell rearrangement is, in addition, coupled with a quadrupolar long-range redistribution of elastic stresses via an Eshelby-type kernel [53–55]. Cells that slip acquire new thresholds; in this way, the mechanical annealing drives a threshold selection process, shaping the mechanical response. Despite their simplicity, these mesoscale models reproduce most of the phenomenology of the plastic behavior of amorphous plasticity upon monotonic loadings, such as avalanches [56], localization [57], and creep [58]. With the development of methods for characterizing local plastic rearrangements and local yield stress [59–62], it has been possible to achieve quantitative agreement between atomistic and mesoscopic simulations [63–66]. In addition, it was recently shown that the reversible plastic behavior observed upon cyclic loading and the associated irreversibility transition could also be reproduced with such type of models [67–69]. Among its other advantages, the discrete nature of mesoscopic models makes them a natural tool to build the transition graphs recently introduced to study and characterize the complex landscape of amorphous solids [21,33,69].

This article is organized as follows. In Sec. II, we give a short description of the quenched mesoscopic elastoplastic model (QMEP), which we introduced recently to study mechanical annealing and memory behavior under oscillatory shear [69]. After defining the training and readout protocols, we verify in Sec. III that the QMEP model can retrieve the amplitude of past oscillatory driving. We analyze sample-to-sample fluctuations under readouts and demonstrate how these fluctuations are connected with the irreversibility transition. In Sec. IV, we provide a detailed analysis of the mechanical properties that the solid acquires at the local scale as a result of annealing. We then show in Sec. V how this leads to memory formation. In particular, we develop readout protocols able to access both the training amplitude and the last direction of return to the trained state. In Sec. VI, we focus on the mechanically annealed state. We analyze our readout results through the lens of return point memory and discuss quantitatively the scenario of an emergence of RPM upon mechanical annealing. In particular, we compare the memory behavior of our model with the predictions of a Preisach-like model based on the sole knowledge of the trained state, which obeys RPM by construction. We conclude by outlining in Sec. VII perspectives that emerge from our work.

II. QUENCHED MESOSCOPIC ELASTOPLASTIC MODEL

The QMEP, first introduced in Ref. [69], follows the spirit of early depinning-like models of amorphous plasticity [70]. The plastic deformation of dense amorphous solids results from a series of localized rearrangements of the disordered structure. These local plastic events are the building blocks of the mesoscopic elastoplastic models [52]. Discretization is performed on a lattice at a mesoscopic length scale, which is large enough to experience a plastic event but still small enough so that only one such event can occur at a time [36,63]. The physics of the model relies on the coupling between local threshold dynamics and an elastic interaction. The latter leads to a redistribution of local stresses whose general features derive directly from the solution of the eigenstrain Eshelby inclusion problem [53]. Part of the complex phenomenology exhibited by EP models is due to the long-range and quadrupolar character of the stress redistribution: depending on the distance and orientation, a plastic event tends to either facilitate or prevent plastic events at distant cells [55,56,71,72]. The mesoscopic nature of the model arises from the fact that the disordered thresholds assigned to each cell emerge from the details of the amorphous structure on a microscopic scale [36,60], while the interaction between the cells is obtained by calculating elasticity on a continuous scale.

Although noise and disorder have been essential ingredients of both mesoscopic elastoplastic models [70,73,74] as well as rheological mean-field models [75,76], implementations and interpretations have been so diverse that, to this day, no clear consensus has emerged on their role and importance in the various features of amorphous plasticity. The role and the importance of structural disorder in rheological and amorphous plasticity models were earlier pointed out in Refs. [70,77]. The relevance of disorder in athermal amorphous materials under shear was further studied analytically and numerically in extensions of the Hebraud-Lequeux model [78–80]. In this context, a key and entirely original feature

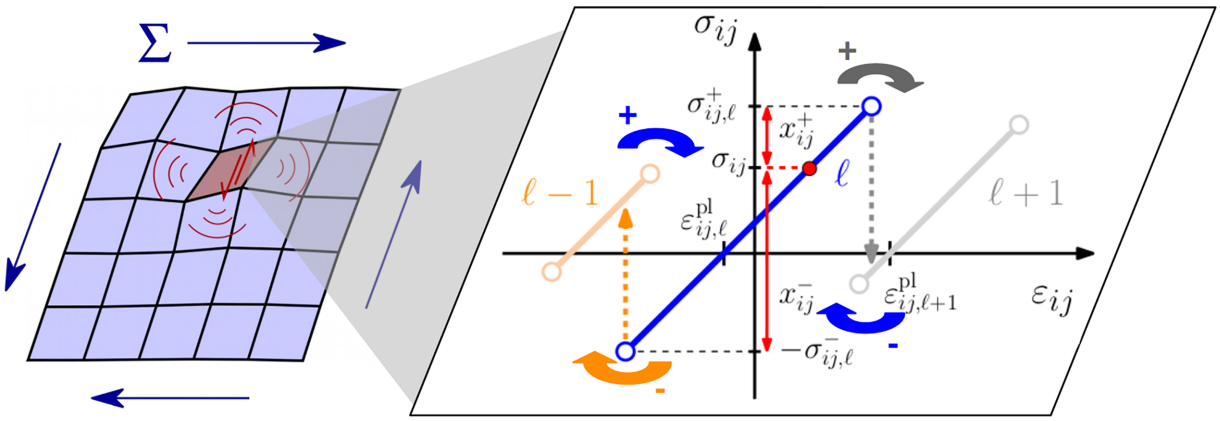

FIG. 1. Mesoscale modeling of an amorphous solid. (Left) Lattice of cells. (Right) The response of each cell (i, j) to external stress Σ consists of a sequence of elastic branches, labeled $\ldots, \ell-1, \ell$ and $\ell+1, \ldots$, which are limited by local stress thresholds in the forward σ^+_{ij} and reverse σ^-_{ij} directions of shear. The collection of all local elastic branches across cells constitutes the quenched disordered landscape of the model. The stability of the cell is characterized by the plastic strengths x^+_{ij}, x^-_{ij}, defined as the distance from the local stress value σ_{ij} to the forward threshold σ^+_{ij} and reverse threshold σ^-_{ij}, respectively.

of the QMEP model introduced in Ref. [69] is the quenched character of the disorder in the plastic thresholds.

A short introduction to the basics of the model in given in Appendix A. We also refer the reader to Refs. [69,81] for a more complete presentation. In the following we focus on the specifics and the details of the implementation of the quenched disorder in Sec. II A and we give the simulations details in Sec. II B.

A. Quenched-disorder landscape

We consider a quenched random distribution of plastic thresholds for a two-dimensional amorphous solid that has been spatially coarse-grained into a $N \times N$ lattice Λ of mesoscale cells indexed as (i, j) and illustrated in Fig. 1. For each cell (i, j), we assign a pair $(\sigma^-_{ij}, \sigma^+_{ij})$ of plastic thresholds that bound the mechanical stability range of the cell and constitute a *local elastic branch*.

The stability criterion simply writes: $-\sigma^-_{ij} < \sigma_{ij} < \sigma^+_{ij}$ where σ_{ij} is the local value of the stress in cell (i, j). The global stress $\Sigma = \sum_{ij} \sigma_{ij}/N^2$ is the spatial average of the local stress field. As shown in Fig. 1, one can also define the local plastic strengths: $x^+_{ij} = \sigma^+_{ij} - \sigma_{ij}$ and $x^-_{ij} = \sigma^-_{ij} + \sigma_{ij}$ which inform us on the distance to instability in the forward and reverse shear directions, respectively.

If upon driving in the *forward (reverse)* direction, the local stress σ_{ij} reaches the upper (lower) bound σ^+_{ij} (σ^-_{ij}) of the elastic branch, or equivalently when $x^+_{ij} = 0$ $(x^-_{ij} = 0)$, then the system gets unstable and jumps toward a new local elastic branch. This branch, in turn, is bounded by its own pair of plastic thresholds drawn from the same random distribution of thresholds as the original one. The quenched disorder we impose was first introduced in Ref. [69] and is illustrated in Fig. 1. We associate to each cell a *stack* of local elastic branches. We label the branches of a stack as $\ldots, \ell-1, \ell, \ell+1, \ldots$, and assume that their properties are *frozen*. This constitutes the (local) stress landscape of a given cell. If after a forward drive, causing the cell to be driven from elastic branch ℓ to $\ell+1$, the system is subject to a reversal of driving direction, then it must first revisit the local elastic branch ℓ with its corresponding stress thresholds. The frozen nature of disorder thus allows for reversible plastic events. Such reversible local plastic events were observed in early molecular dynamics simulations and experiments by Lundberg *et al.* [82]. Let us stress however that while at the level of single local elastic branches the yields events are reversible, this is not necessarily true at the global level, i.e., when we consider the response to an externally applied shear. The transition from one global elastic branch to another upon strain increase will in general not cause the system to return to the previous branch upon subsequent decrease of strain, as the cells triggering these instabilities leading to the transitions will be not the same and hence give rise to different plastic events.

To characterize the distinct stress landscapes seen by the individual cells (i, j), we label their local elastic branches as ℓ_{ij} so that the local branch configuration of all cells of the lattice is given by the collection of integers $(\ell_{ij})_{(i,j)\in\Lambda}$. We can think of the triplet (i, j, ℓ_{ij}) as a 3D embedding of the 2D lattice Λ of mesoscopic cells [56,71]. This triple, in turn, establishes the local elastic branches via the parameters such as $(\sigma^-_{ij,\ell_{ij}}, \sigma^+_{ij,\ell_{ij}})$. Thus, regarding the 3D embedding, the latter are quenched random variables. When projected down to the 2D lattice of cells (i, j), the local branch index ℓ_{ij} acts like the height function of an elastic interface evolving in a *quenched* disordered landscape [56,69,71]. This point of view was discussed further in Ref. [66].

B. Sample preparation and simulation details

The initial condition, i.e., the initial value of the plastic thresholds $\sigma^{\pm}_{ij}$ and local stress fields σ_{ij}, is obtained after a randomizing sequence of effective thermal and aging steps. By varying the thermalization and aging protocol, we can tune the systems' effective age and mechanical behavior from the poorly aged and very ductile case to the very aged and highly brittle case. In the following, we restrict our study to poorly aged (PA) samples, whose preparation protocol has been

described in Refs. [69,81]. This preparation protocol is chosen to ensure that the system deforms plastically in a statistically homogeneous manner without exhibiting stress overshoot and strain localization. This allows memory effects to be studied at low shear amplitudes while avoiding trivial elastic behavior in deeply quenched, hard glasses.

At the end of the preparation process, the plastic strain is conventionally set to zero, i.e., we define $\ell_{ij} \equiv 0$ for the local branch configuration all cells (i, j). This defines the state obtained after preparation as the initial condition for the subsequent mechanical annealing of the samples by shear. The latter is done under athermal and quasistatic conditions [83].

We simulated systems of size 16×16, 32×32 and 64×64, and used a Weibull distribution for the thresholds: $P(\sigma^{\pm}) = 1 - e^{-(\sigma^{\pm}/\lambda)^{\kappa}}$ with $\kappa = 2$ and $\lambda = 0.1$. Note that stress values are rescaled with the shear modulus μ. The plastic strain increment $\Delta\varepsilon = \varepsilon^{pl}_{ij,\ell+1} - \varepsilon^{pl}_{ij,\ell}$ between two neighbor elastic branches ℓ and $\ell + 1$ is also a random variable. We choose it to be correlated to the two stress thresholds associated with the transition $\ell \to \ell + 1$: $\Delta\varepsilon$ is drawn from a uniform distribution in $[0, \Delta\varepsilon_{\max}]$. $\Delta\varepsilon_{\max} = \eta(\sigma^{+}_{ij,\ell} + \sigma^{-}_{ij,\ell+1})/2$ where the division by 2 comes from the elastic relation $\sigma/2\mu = \varepsilon$. The maximum $\Delta\varepsilon_{\max}$ is chosen to maintain consistency in plastic jumps between branches, ensuring nonzero overlap between the successive elastic branches that constitute the stress landscape. The tunable parameter η controls the strength of the elastic interaction, and we set $\eta = 1$ [69,81].

III. MEMORY OF AMPLITUDE OF PAST OSCILLATORY SHEARING

To investigate memory behavior, the systems are first subjected to a *training protocol* followed by a *readout protocol*. Here, we discuss the reversible plastic behavior that can be obtained upon training by applying cyclic shear. We then present two different readout protocols and discuss their performance in retrieving the amplitude of the training protocol. We finally discuss the fluctuation behavior of the readout response and link it to the irreversibility transition.

A. Oscillatory training: Reversible plasticity and the irreversibility transition

The training protocol consists of a sequence of $\mathcal{N}_T$ shear cycles of oscillatory shear $0 \to \varepsilon_T \to -\varepsilon_T \to 0$, where ε_T is the amplitude. In Ref. [69], we investigated the evolution of the QMEP model toward cyclic response under oscillatory shear. The system quickly locks into a limit cycle at low training amplitudes, and the response is perfectly elastic. This behavior continues up to a shear amplitude $\varepsilon_{\rm hys}$, where a hysteresis loop opens up, and plasticity emerges, albeit in a *reversible* way [9,67,82,84]: as the limit-cycle is traversed, the sequence of plastic events takes place in such a way as to precisely compensate each other so that at the end of the limit-cycle, the system has returned to the same configuration as at its beginning. This means that the same sequence of plastic events repeats from cycle to cycle, hence the term *reversible plasticity* [82]. Beyond the hysteresis transition $\varepsilon_{\rm hys}$, the number of training cycles needed to reach reversibility gets larger with increasing amplitude ε_T [84]. At the same time, the eventually attained limit-cycles involve an increasingly larger number of plastic events, while the periodicity of the cyclic response starts to span multiple driving cycles—a phenomenon called multiperiodicity or subharmonicity [85,86]. We will use *monoperiodic* to emphasize that the cyclic response period coincides with that of the driving.

A cyclic response is attainable up to a strain amplitude $\varepsilon_{\rm irr}$. This marks the onset of the *irreversibility transition* beyond which no limit cycle can be found, and diffusion starts to take place [13,14,16]. In Ref. [69], we defined $\varepsilon_{\rm irr}$ in a statistical way. Given a maximum number $\mathcal{N}_T$ of driving cycles, $\varepsilon_{\rm irr}$ is the training strain amplitude at which 50% of the realizations lead to a cyclic response. The amplitude $\varepsilon_{\rm hys}$, marking the transition from purely elastic to plastic cyclic response, is defined similarly.

While we present only results obtained from poorly aged (PA) realizations of size 16×16, we would like to note that qualitatively similar responses were also obtained for PA systems of sizes 32×32 and 64×64. For the 16×16 PA glasses we chose $\mathcal{N}_T = 10^4$ and find that $\varepsilon_{\rm hys} = 0.025$ and $\varepsilon_{\rm irr} = 0.0689$. Unless otherwise noted, all results to be shown are averages obtained from 10^3 realizations of trained glasses.

B. Readout protocols: Implementation and results

The trained samples are subjected to a *readout protocol* in which we apply a single cycle of oscillatory shear at *readout amplitude* ε_R. As described below, we then characterize the proximity of the states of our glass before and after the readout, labeling these as T and R, respectively. Experimentally, a *sequential* readout protocol is typically used [1,2,10]. This consists of applying to the trained state T a sequence of shear cycles of increasing amplitude ε_R. At the end of each cycle, the system's state is compared with T. Numerically, it is also possible to resort to a *parallel* readout protocol, which consists of taking multiple replicas of the trained state T and applying to each a single cycle of oscillatory shear with some amplitude ε_R [19]. The state R that each replica attains at the end of its readout cycle is then compared with the trained state T. Empirically, for both training protocols, maximum proximity between trained and readout configurations occurs when $\varepsilon_R \approx \varepsilon_T$. In this sense, the trained system retains a memory of ε_T, which subsequently can be read out [1].

In particle simulations and experiments on colloidal suspensions, the proximity between the configurations T and R is quantified by the particles' mean-square displacement (MSD), which involves comparing a set of real numbers that specify the coordinates of the particles. A nice feature of the QMEP model is that a set of integers, the collection $(\ell_{ij})_{(i,j)\in\Lambda}$, fully specifies the configuration. Here, ℓ_{ij} specifies the local branch of cell (i, j) and also counts the number of slips experienced by each cell (i, j), relative to the freshly prepared untrained glass for which $\ell_{ij} = 0$. As introduced in Ref. [81] we then define a distance $d(R, T)$ between two configurations T and R as a Hamming distance between their elastic branch configurations $T = (\ell^{T}_{ij})_{(i,j)\in\Lambda}$ and $R = (\ell^{R}_{ij})_{(i,j)\in\Lambda}$:

$$d(R, T) = \frac{\left|\left\{(i, j) \in \Lambda : \ell^{R}_{ij} \neq \ell^{T}_{ij}\right\}\right|}{|\Lambda|}, \tag{1}$$

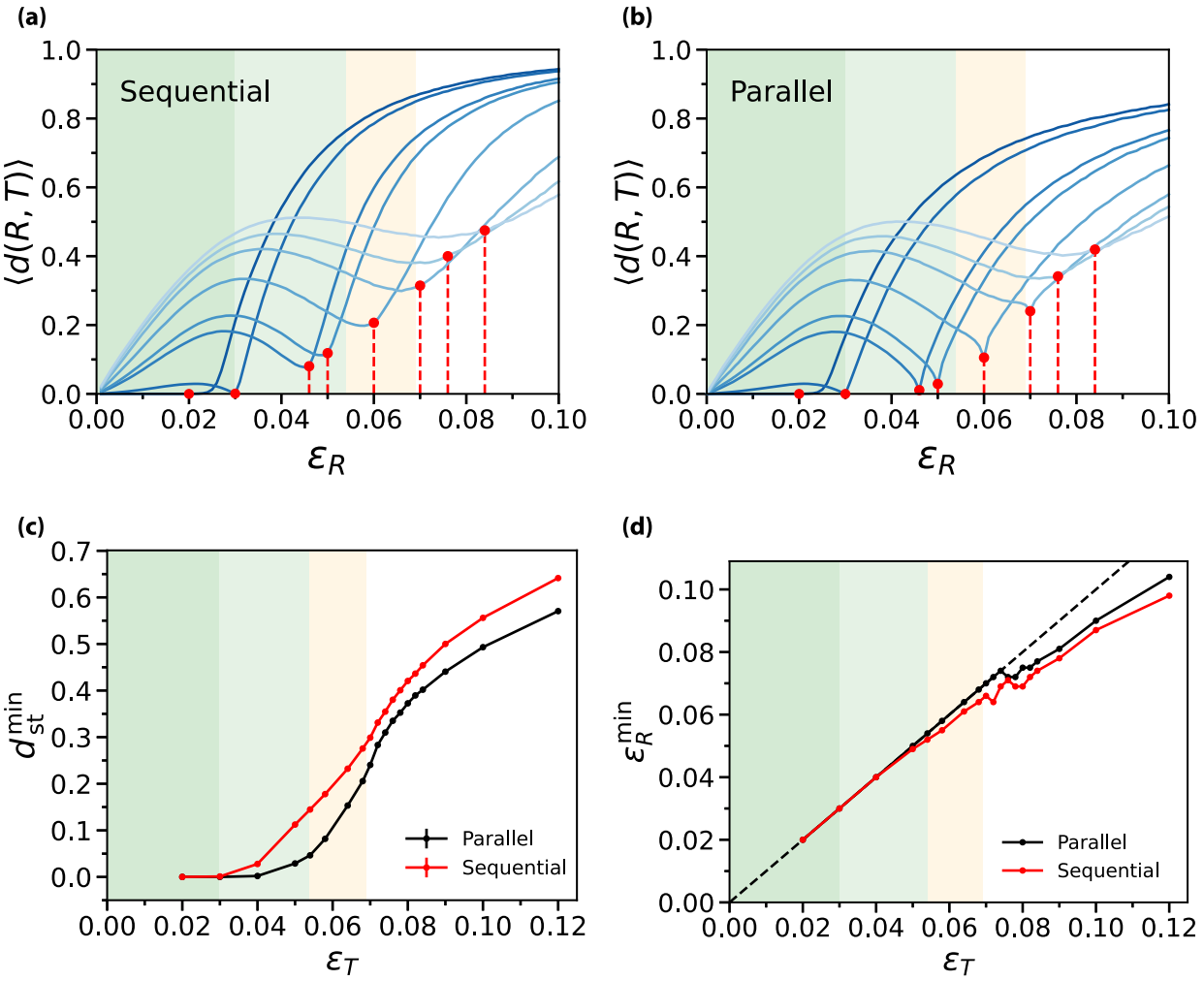

FIG. 2. Memory response of the QMEP model after training by application of oscillatory shear at strain amplitude ε_T. Readout response for (a) sequential and (b) parallel readout protocol; (c) evolution of the minimum stroboscopic distance $d_{\rm st}^{\rm min}$ over a readout protocol with the training amplitude ε_T; (d) evolution of the strain amplitude $\varepsilon_R^{\rm min}$ with the training amplitude ε_T. $\varepsilon_R^{\rm min}$ is the readout amplitude at which the local minimum of the stroboscopic distance $d_{\rm st}^{\rm min}$ is attained. Background colors indicate the different regimes of reversibility. Dark green: all realizations lock into a monoperiodic cycle; light green: all the limit cycles are mono or multiperiodic; orange: some realizations do not reach a limit cycle, i.e., reversible response; white: above the irreversibility transition. Refer to the text for further details.

where $|\Lambda| = N^2$ is the number of cells of the mesoscale model, and $|A|$ counts the number of elements of a set A. The distance $d(R, T)$ thus varies between 0 for identical configurations and 1 for configurations so distinct that they do not overlap on any of the cells.

In Figs. 2(a) and 2(b), we show the evolution of the stroboscopic distance with readout amplitude ε_R for a set of trained states and the cases of sequential and parallel readout protocols. The training amplitudes ε_T chosen vary from 0.02 to 0.085 and have been marked by vertical dashed lines whose termination on the corresponding readout curve is indicated by a red circle. For the lowest training amplitudes $\varepsilon_T = 0.02$, the readout distance $d(R, T)$ vanishes for $\varepsilon_R \lesssim \varepsilon_T$, and the resulting response cycles are perfectly elastic, with all cells remaining in their local elastic branches. At higher readout amplitudes, $d(R, T)$ exhibits nonmonotonic behavior with ε_R developing a clear local minimum close to the value of the training amplitude. The same observations also hold in the case of parallel readouts, shown in Fig. 2(b). Our QMEP model thus reproduces well the memory features recently observed in particle simulations and experiments [11,12,18–20,22,23,25,26]. Note that since, in the case of parallel readout, the shear cycles are applied to replicas of the trained state T, there is no accumulation of stroboscopic distances due to the prior readout cycles, as is the case for sequential readouts. This is why minima observed under parallel readout are sharper and more clearly defined.

We turn next to characterising the quality and accuracy of recovering the training amplitude from the readout. We first focus on the behavior of the readout distance $d_{\rm st}^{\rm min}$ at the local minimum of $d(R, T)$. As illustrated in Fig. 2(c), for both sequential and parallel readout, we observe that $d_{\rm st}^{\rm min}$ departs from zero and gradually increases with the training amplitude. The background colors refer to different regimes identified in Ref. [81] and give us a guide to better understanding the evolution of $d_{\rm st}^{\rm min}$. The leftmost region, shaded in

dark green, indicates the range of training amplitudes where all systems attain limit-cycles, and their response is monoperiodic. Hence, we expect that $d_{\rm st}^{\rm min} = 0$ in this regime. The middle region, shaded in light green, indicates the range of training amplitudes where all systems attain limit-cycles, but some of these are multiperiodic, i.e., their period spans two or more driving cycles. The slow increase of $d_{\rm st}^{\rm min}$ in this range is entirely due to the gradual emergence of complex limit cycles with increasingly longer periods [67,69,81]. In the case of multiperiodic response, since the readout protocol consists of a single cycle only, the trained and read configurations are no longer identical. Finally, the right region, shaded in orange, indicates the range of training amplitudes where some samples fail to attain cyclic response during the prescribed duration of $\mathcal{N}_T$ applied training cycles. Here, we find that the fraction of trained samples attaining cyclic response decreases with increasing ε_T. The upper limit of this regime is marked by the onset of the irreversibility transition $\varepsilon_{\rm irr}$, which we had defined earlier as the training amplitude at which half of the samples reach a limit cycle. Beyond this regime, a fraction of the samples still manages to attain cyclic response, so a shallow minimum is still observable.

Next, we quantify the accuracy with which the sequential and parallel readout protocols can infer the trained strain ε_T. Denote by $\varepsilon_R^{\rm min}$ the value of the readout strain ε_R at the local minimum $d_{\rm st}^{\rm min}$ of the readout $d(R, T)$, cf. Figs. 2(a) and 2(b). In Fig. 2(d) we plot $\varepsilon_R^{\rm min}$ against the trained amplitude ε_T. The dashed line $\varepsilon_R^{\rm min} = \varepsilon_T$ serves as a guide to the eye. We observe that for parallel readouts (black symbols) and up to the irreversibility transition, $\varepsilon_R^{\rm min}$ furnishes a rather precise estimate of the training amplitude. This behavior extends to even slightly larger values of ε_T. In contrast, for the sequential readouts, the precision of the measurement gradually degrades as the training amplitude increases.

C. Fluctuations of the readout response unveils the irreversibility transition

We now discuss the sample-to-sample fluctuation behavior of the memory readout. For simplicity, we restrict ourselves to the case of parallel readouts. In Fig. 3 we show the variance $V(\varepsilon_R, \varepsilon_T)$ of the stroboscopic distance $d(R, T)$ under parallel in-phase readouts and for an ensemble of samples prepared at training amplitudes ε_T with subsequent readouts at ε_R.

We start with the behavior of $V(\varepsilon_R, \varepsilon_T)$ with ε_R when ε_T is small. From Fig. 3(a) we see that for $\varepsilon_T = 0.03$, the variance $V(\varepsilon_R, \varepsilon_T)$ exhibits a minimum when $\varepsilon_R = \varepsilon_T$ and actually vanishes there. As can be seen from Fig. 2(b), the vanishing of V at $\varepsilon_R = 0.03$ reflects the fact that for low training amplitudes, all realizations are locked into monoperiodic limit cycles. Increasing ε_R further, the variance peaks just after ε_T and then decreases gradually. This decrease is related to the bounded character of the stroboscopic distance $d_{\rm st} \in [0, 1]$. For large values of ε_R, the stroboscopic distance gradually approaches its upper bound $d_{\rm st} = 1$. Hence, sample-to-sample fluctuations get smaller again, and the variance $V(\varepsilon_R, \varepsilon_T)$ decreases.

Interestingly, the behavior of $V(\varepsilon_R, \varepsilon_T)$ with ε_R gets significantly modified when the training amplitude ε_T is increased further: at first, a sharp minimum at $\varepsilon_R \approx \varepsilon_T$ prior to the peak

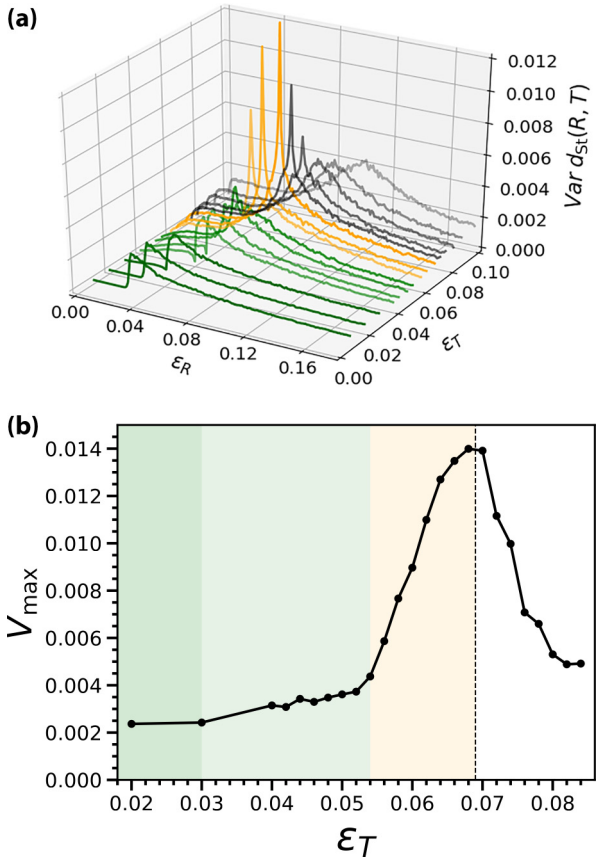

FIG. 3. Sample-to-sample fluctuations in the readout. (a) Variance of the readout response over an ensemble of 10^3 realizations in its dependence on readout amplitude ε_R for various training amplitudes ε_T. The variance exhibits a maximum for the training amplitudes shown when $\varepsilon_R \approx \varepsilon_T$. The global maximum of the variance is attained near the strain $\varepsilon_{\rm irr}$, marking the onset of the irreversibility transition, $\varepsilon_R \approx \varepsilon_T \approx 0.07$. Line colors reproduce the choice background colors described in the caption of Fig. 2 and label the different regimes of reversibility. (b) Maximum of variance $V_{\rm max}(\varepsilon_T)$ of the stroboscopic distance $d(\varepsilon_R, \varepsilon_T)$ as a function of the training amplitude ε_T. $V_{\rm max}(\varepsilon_T)$ shows a maximum at $\varepsilon_T \approx \varepsilon_{\rm irr}$.

emerges. With increasing ε_T, this minimum gradually disappears while the peak becomes sharper. A global maximum of $V(\varepsilon_R, \varepsilon_T)$ *is observed* when $\varepsilon_R \approx \varepsilon_T$ is around $\varepsilon_{\rm irr}$. When ε_T is increased further, the maximum of V (as a function of ε_R) starts to broaden again.

The change of behavior of $V(\varepsilon_R, \varepsilon_T)$ along the line $\varepsilon_R = \varepsilon_T$ reflects the increasing complexity and the gradual disappearance of the limit cycles at high training amplitude. Upon increasing the training amplitude, more and more realizations reach a multiperiodic limit cycle or do not reach a limit cycle at all so that the distribution of the distance $d(\varepsilon_T, \varepsilon_T)$ gets bimodal and its variance increases.

For a given training amplitude ε_T, let $V_{\rm max}(\varepsilon_T)$ be the maximum variance reached as the readout amplitude changes. As already noted above, and shown in Fig. 3(b), we observe a well-defined peak of $V_{\rm max}(\varepsilon_T)$ near the irreversibility transition, i.e., when $\varepsilon_T \approx \varepsilon_{\rm irr} = 0.0689$. The emergence of this maximum of fluctuations stems directly from the definition of the irreversibility transition. At $\varepsilon_T = \varepsilon_{\rm irr}$, half of the

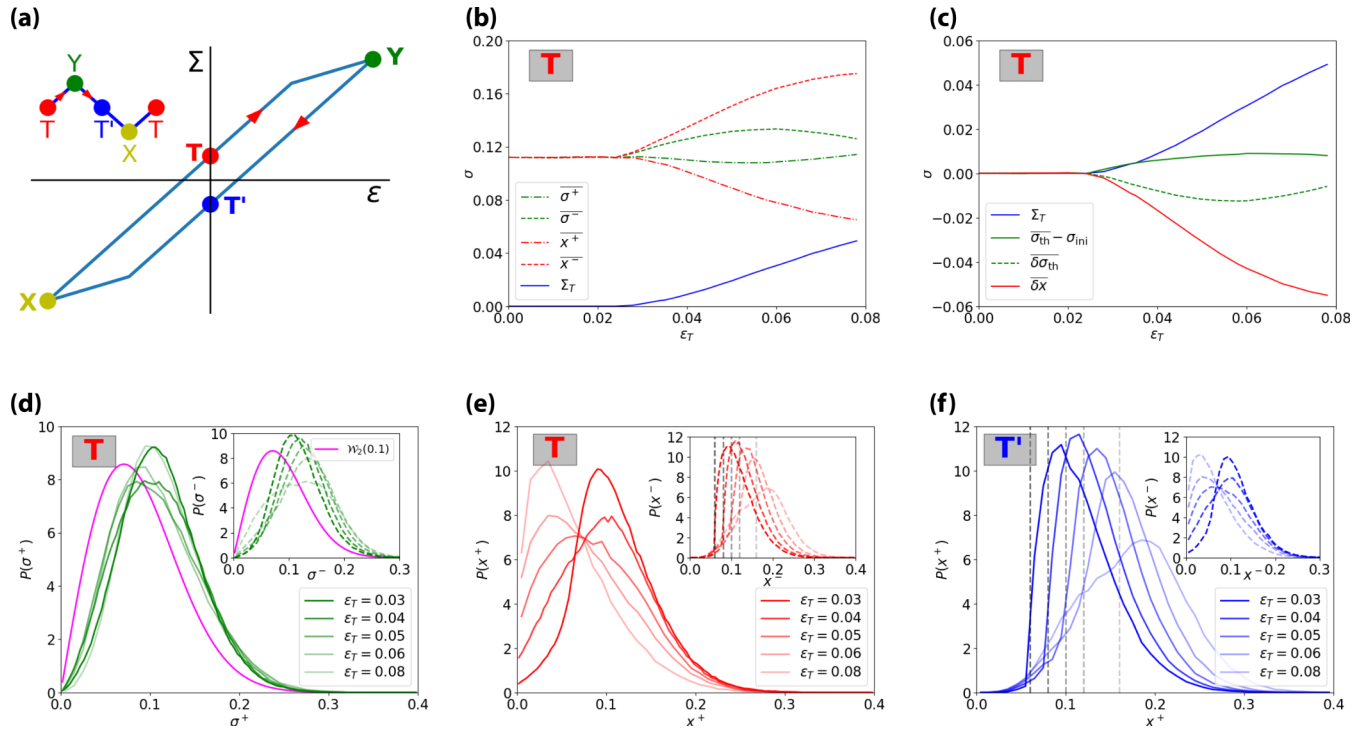

FIG. 4. Emergence of anisotropy and parity as a result of training. (a) Sketch of the stress-strain relation of a monoperiodic limit-cycle under applied oscillatory shear $0 \to \varepsilon_T \to 0 \to -\varepsilon_T \to 0$. Red arrows indicate the sense of orientation. The sequence of local elastic branch configurations visited during the cycle is $T \to Y \to T' \to X \to T$. (b), (c) The behavior with training amplitude ε_T of sample-averaged properties of local elastic branches ℓ_{ij} of cells (i, j) in the trained state T: (b) Sample-averaged local stress thresholds $\overline{\sigma^{\pm}}$, plastic strengths $\overline{x^{\pm}}$ and residual stress Σ_T. (c) Training-induced hardening of local elastic branches relative to untrained samples, as quantified by $\overline{\sigma_{\rm th}} - \sigma_{\rm ini}$ where $\overline{\sigma_{\rm th}} = \overline{(\sigma_{ij}^+ + \sigma_{ij}^-)}/2$. The plot also shows the average anisotropies in local stress thresholds $\overline{\delta\sigma_{\rm th}} = \overline{(\sigma_{ij}^+ - \sigma_{ij}^-)}/2$ and plastic strengths $\overline{\delta x} = \overline{(x_{ij}^+ - x_{ij}^-)}/2$. Note that all four quantities coincide up to the hysteresis transition $\varepsilon_{\rm hys} = 0.025$, marking the onset of plasticity. (d) The main figure and the inset show the distribution of forward and reverse local stress thresholds at T, i.e., σ^+ and σ^-, respectively. The purple curve corresponds to the quenched disorder stress threshold, given by the Weibull distribution $w_2(0.1)$. (e), (f) The distributions of local plastic strengths x^+ (main figure) and x^- (inset) at states T and T' of the cyclic response. The dashed vertical lines are located at $2\varepsilon_T$.

realization lock-in into a limit cycle while the other half does not. Therefore, the stroboscopic distance follows a bimodal distribution of $d(R, T)$ whose low (high) values indicate the presence (absence) of limit cycles. This result demonstrates that the irreversibility transition can be directly identified from the sample-to-sample fluctuation behavior of the readout protocol.

IV. EMERGENCE OF TRAINING-INDUCED STRUCTURAL ANISOTROPY

Shear plasticity induces stress and structural anisotropy. The existence of a residual strain classically defines plasticity as a result of loading a system and subsequently unloading it back into a stress-free condition. The return to an unstrained state then requires the application of a nonzero global stress, corresponding to a *residual stress*. Plasticity within a training cycle (hysteresis) is thus expected to induce stress anisotropies. Interestingly, in addition to this *macroscopic* effect, shear plasticity also induces similar structural anisotropies at the *microscopic* scale. These have been observed in the alignment of polymer chains, the anisotropy of networks of granular contacts [87], as well as in silica atoms [88–90], and can be quantified by nematic order parameters. At *mesoscopic scales*, the emergence of plasticity-induced anisotropies can be probed by the directional polarization of the distribution of local yield stresses [63,69,81,91], pointing to the central role of the forward-backward asymmetry of the plastic strength distributions in the limit $x^{\pm} \to 0$, which form a pseudogap upon unloading.

Figure 4(a) is a sketch of a monoperiodic stress-strain limit cycle under oscillatory shear. As the applied shear strain varies as $0 \to \varepsilon_T \to 0 \to -\varepsilon_T \to 0$, the system traces out a hysteresis loop given by the branch configurations $T \to Y \to T' \to X \to T$, as shown. We will denote the global residual stresses at T and T' as Σ_T and $\Sigma_{T'}$, respectively.

In Fig. 4(b) we show how the global stress Σ_T as well as the average local stress thresholds $\overline{\sigma^+}$, $\overline{\sigma^-}$ and local plastic strengths at T, $\overline{x^+}$ and $\overline{x^-}$, vary with training amplitude ε_T. Averages have been performed over all cells (i, j) in the state T and across 300 realizations of glasses. All local quantities coincide up to an amplitude $\varepsilon_T = \varepsilon_{\rm hys} = 0.025$, up to which the response is purely elastic and hence the global stresses at T and T' vanish, i.e., $\Sigma_T = \Sigma_{T'} = 0$. The common value of $\sigma_{\rm ini} = 0.112$, which we observe for the stress thresholds and the plastic strengths, is the mean value of the stress threshold distribution of the freshly aged but not yet trained glasses.

Once ε_T becomes larger than $\varepsilon_{\rm hys}$, a residual stress Σ_T starts to build up. In parallel, the plastic events triggered by the driving lead to a *dynamical selection* of local elastic branches, leading to an average local stress threshold that starts to systematically deviate from $\sigma_{\rm ini}$. As apparent from Fig. 4(b), this deviation depends on the sense of the threshold relative to the driving direction. The local stress thresholds $\overline{\sigma^{\pm}}$ shown are measured at T, i.e., when the applied strain is increasing in the *forward* direction. With increasing training amplitude ε_T, $\overline{\sigma^-}$ increases, whereas $\overline{\sigma^+}$ decreases relative to $\sigma_{\rm ini}$. A similar, but more pronounced behavior is observed for the mean plastic strengths $\overline{x^+}$ and $\overline{x^-}$, since these also depend on the residual stress: $\overline{x^+} = \overline{\sigma^+} - \Sigma_T$ and $\overline{x^-} = \overline{\sigma^-} + \Sigma_T$. We find that the mean plastic strengths $\overline{x^+}$ in the forward direction are smaller than those in the reverse direction. This implies that at T the change in applied strain necessary to trigger a plastic event in the forward direction is smaller than in the reverse direction of shearing.

The contrasting distributions of forward and backward thresholds after training indicate the development of structural anisotropy. In Fig. 4(c), we focus in more detail on this training-induced hardening and polarization behavior. We show the evolution with training amplitude of the average of the forward and backward stress thresholds $\overline{\sigma_{\rm th}} = (\overline{\sigma^+} + \overline{\sigma^-})/2$ relative to its initial value, $\sigma_{\rm ini}$, as well as those of the polarizations of thresholds and plastic strengths: $\overline{\delta\sigma_{\rm th}} = (\overline{\sigma^+} - \overline{\sigma^-})/2$ and $\overline{\delta x} = (\overline{x^+} - \overline{x^-})/2$. As a reference scale, we also plot the residual stress's evolution Σ_T. As expected, we observe a polarization effect: both $\overline{\delta\sigma_{\rm th}}$ and $\overline{\delta x}$ depart from zero above the hysteresis transition. In addition, we also observe a significant hardening effect: the mean thresholds $\overline{\sigma_{\rm th}} = (\overline{\sigma^+} + \overline{\sigma^-})/2$ tend to get higher upon training. In other words, the extent of the local elastic branches (their stability range) increases. Interestingly, the evolution of both the hardening as well as the polarization of thresholds is nonmonotonic. A peak is observed around $\varepsilon_T \approx 0.55$, the value above which not all systems find limit cycles anymore. In contrast, due to its dependence on residual stress, the plastic strength polarization $\overline{\delta x} = \overline{\delta\sigma_{\rm th}} - \Sigma_T$ keeps increasing with the training amplitude ε_T.

Figure 4(d) shows the distribution of the stress-thresholds σ^+ in state T, whose averages $\overline{\sigma^+}$ have been depicted in Fig. 4(b), for $\varepsilon_T = 0.03, 0.04, 0.05, 0.06$, and 0.08. Note that the last value is above the irreversibility transition $\varepsilon_{\rm irr} = 0.0689$. The distribution in purple is the a priori Weibull distribution of thresholds employed to build the quenched disorder. The slight decrease of $\overline{\sigma^+}$ with ε_T in Fig. 4(b) is seen to be predominantly due to an asymmetric broadening of the distributions. The distributions of σ^-, presented in the inset of Fig. 4(d), exhibit a rather different behavior. With increasing ε_T, the shapes of the distributions largely remain the same while their peak is moving systematically toward larger values. The dynamical selection process that gives rise to the distribution of stress thresholds in state T thus appears to operate mainly on reverse thresholds σ^-. Note here that the emergence of anisotropy and the hardening of the thresholds provides a strong evidence that the quenched character of the disordered landscape does not impede the evolution/adaption processes that take place on it.

The main panel and inset of Fig. 4(e) shows the distribution of plastic strengths x^+, respectively x^- at T. The vertical dashed lines in the insets correspond to the values $x_T = 2\varepsilon_T$, the elastic stress associated with a shear strain ε_T (we remind here that stresses are rescaled by the shear modulus μ so that the elastic behavior in shear simply is $\sigma = 2\varepsilon$). Notice the increase of asymmetry of the distributions of $x^{\pm}$ at T as ε_T increases. While the distribution of x^+ starts to have an increasing number of cells with low plastic strengths, the corresponding population of such cells in the distribution of x^- gets increasingly smaller. In particular, for the latter, a sharp front emerges at x_T, below which only a relatively small population of weak sites persists (note that these x^- values below x_T gradually build up a generic distribution when x_T increases). This is a first hint of the emergence of a mechanical memory at the mesoscopic scale. The value of the training amplitude gets imprinted as a clear feature in the distribution of plastic strengths. Note that at the higher training amplitude $\varepsilon_T = 0.08$—which is above $\varepsilon_{\rm irr}$—the front at x_T has almost entirely disappeared.

Figure 4(f) shows the distribution of plastic strengths at the antipode T' of the limit cycle where the applied strain is again zero but decreasing. The plastic strengths in the direction of shearing are now given by x^-. In fact, for the training amplitudes shown, the distributions of $x^{\pm}$ at T and $x^{\mp}$ at T' are statistically identical. Given that the full cycle of applied shear returns the system back to its initial strain, these findings imply that the branches $X \to T \to Y$ and $Y \to T' \to X$ under increasing and decreasing shear, respectively, are also statistically indistinguishable under reversal of shear directions. Thus, we have a parity operation that maps the statistical properties of the two branches and, hence, the corresponding antipodal states T and T' into each other. Let us emphasize that this parity *emerges* due to the cyclic shearing. Moreover, this parity persists even at large shear amplitudes where a cyclic response is not attainable anymore.

Oscillatory training thus induces two complementary effects on the glass structure. First we observe a mechanical annealing effect: upon increasing training amplitude, the mean stress thresholds $\overline{\sigma^{\pm}}$ increase, the glass hardens and gets more stable. The hardening shows a maximum around the irreversibility transition. This observation is consistent with the observation of a minimum of energy at the irreversibility transition reported in Refs. [50,51,68,80,92–94]. Second, a symmetry breaking emerges between the strain-free configurations of the increasing and decreasing branches of the hysteresis cycle. The distribution of stress thresholds $\sigma_{ij}^{\pm}$ and plastic strengths $x_{ij}^{\pm}$ show mirroring anisotropic distributions. In configuration T, forward stress thresholds σ_{ij}^{+} and plastic strengths x_{ij}^{+} are lower than their reverse counterparts. As a result, on the increasing branch, the glass is softer in the forward direction than in the reverse direction. The opposite statements apply in the strain-free configuration T' of the decreasing branch of the hysteresis cycle. The emergence of this symmetry breaking is accompanied by the formation of a pseudogap in the distribution of plastic strengths opposite to the applied shear direction, while no such pseudogap appears along the shear direction. This phenomenon closely resembles the origin of the Bauschinger effect in amorphous solids, as

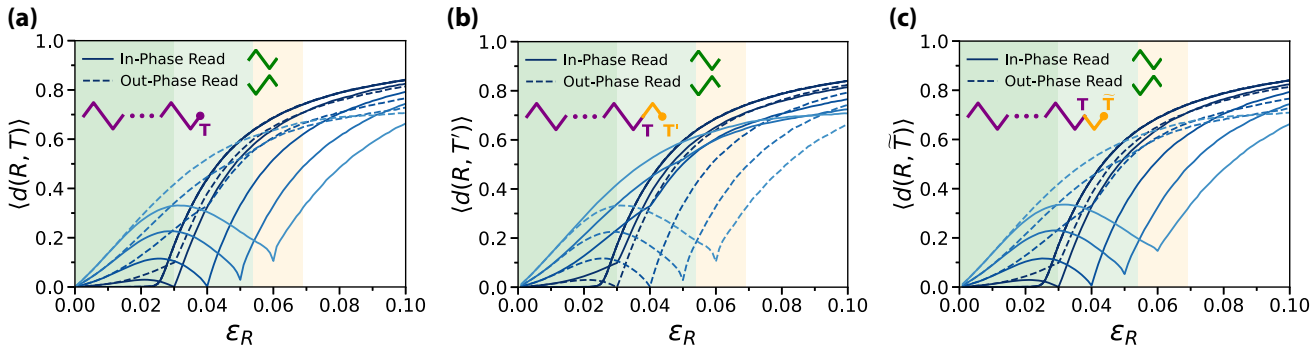

FIG. 5. Memory of shear direction. (a) The effect of applying to the trained state T the parallel readout $0 \to \epsilon\varepsilon_R \to 0 \to -\epsilon\varepsilon_R \to 0$, either in-phase ($\epsilon = 1$) or out-of-phase ($\epsilon = -1$). Shown are the results for training amplitudes $\varepsilon_T = 0.02, 0.03, 0.04, 0.05$, and 0.06 (in decreasing shades of blue). The in-phase readouts (solid lines) exhibit a strong memory of training amplitudes; the out-of-phase readouts (dashed lines) do not show strong signs of memory. (b) Parallel in- and out-of-phase readouts applied to state T', reached from T by adding an in-phase half-cycle, as indicated in legend. Contrary to panel (a), here, the in-phase readouts (solid lines) do not exhibit a strong memory of training amplitudes, while the out-of-phase readouts (dashed lines) exhibit cusps at the training amplitudes. Modulo phase, the readouts from T' are quantitatively similar to those applied to T depicted in panel (a), supporting the antipodal nature of T and T'. (c) Parallel in- and out-of-phase readout performed on the state $\bar{T}$, obtained by applying an additional out-of-phase training half-cycle $0 \to -\varepsilon_T \to 0$ to T.

demonstrated in Refs. [63,91]. Notably, the width of the pseudogap in the reverse plastic strength distribution is precisely $2\varepsilon_T$, corresponding to the elastic stress associated with the training amplitude ε_T. In mean-field models, such gaps arise by construction, as it is assumed that the cyclic response of the mesoscale blocks is purely elastic, which implies that $x^{\pm} > x_T$ for each block [80,93,94]. In our model, these features emerge by themselves as a result of the mechanical annealing.

Our results show that the interplay between forward and reverse plastic strengths is rather complex, and that under cyclic response gaps in the distribution of local plastic strengths open and close as the driving changes direction. These features can be regarded as a microscopic imprint of the oscillatory training on the glass structure, encoding thereby mechanical memory.

V. MEMORY OF THE LAST DIRECTION

We have seen that oscillatory training of an amorphous solid induces the emergence of an anisotropic order at the mesoscopic scale. Upon cyclic shearing, the amorphous structure oscillates between two well-defined polarized states. To what extent can this structural imprint be used to readout a mechanical memory? In this section, we show that the classical readout protocols are actually highly sensitive to the last direction of shear driving. We propose a readout protocol that gives access to both the amplitude and the direction of the oscillatory training. After the parallel version, we introduce a sequential version of the readout protocol, which should be experimentally applicable.

A. In- and out-of-phase readout protocols

Defining the *in-phase* readout protocol as $0 \to s\varepsilon_R \to 0 \to -s\varepsilon_R \to 0$, where $s = 1$, we will refer to the case when $s = -1$ as an *out-of-phase* readout. Figure 5(a) shows the result of applying parallel in- and out-of-phase readouts to states T of samples trained at amplitudes $\varepsilon_T = 0.02, 0.03, 0.04, 0.05$, and 0.06. As we have already seen in Fig. 2(b), the in-phase readouts in Fig. 5(a) (solid lines) exhibit a strong memory of the training amplitude, which is evidenced by the pronounced local minima of $d(R, T)$ where the readout amplitude matches the training amplitude. The out-of-phase readouts shown in Fig. 5(a) (dashed lines) exhibit a less pronounced memory that is only revealed by a change of slope of $d(R, T)$ around $\varepsilon_R \approx \varepsilon_T$ and gets weaker with increasing training amplitude.

Figure 5(b) shows the result of applying parallel in- and out-of-phase readouts to the state T', which is reached from T under the application of an *additional* (in-phase) half-cycle $0 \to \varepsilon_T \to 0$ [see also the sketch in Fig. 5(b)]. We see that the in-phase readouts now do not bear a strong memory of the training, while the out-of-phase readouts clearly do. Moreover, modulo readout-phase, these two sets of readout curves are quantitatively similar. This finding is consistent with the notion of parity and the states T and T' being antipodal, as discussed in the previous section. Thus, parity applies not only to the distributions of local stress thresholds and plastic strengths, which are static quantities associated with states T and T', but also to families of microscopic deformation pathways during readouts.

B. Memory of direction of shear

Note that the readouts at T or T' will recover the memory of the training amplitude only if we apply the correct readout phase. However, the statistical invariance under the exchange of T with T' in combination with a switch of shearing direction implies that the memory can only be retrieved by a readout if it is in phase with the last direction of shear.

Consider now an out-of-phase readout. It can be decomposed into two consecutive half-cycles: the first one toward the negative strains and the second one toward the positive strains. Due to the training-induced anisotropy, we expect these two half cycles to show contrasting effects. In particular, if we examine the inset of Fig. 4(e), we note the existence of a gap of width $2\varepsilon_T$ in the distribution of negative plastic strength, $P(x^-)$. We thus expect an elastic behavior in the

negative strain domain, provided that the maximum strain remains below the training amplitude ε_T; in other words, the system does not traverse the pseudogap.

Let us call $\widetilde{T}$ the state we obtain by subjecting the trained state T to an out-of-phase half-cycle of amplitude ε_T : $0 \to -\varepsilon_T \to 0$. Since we expect a nearly elastic behavior between T and $\widetilde{T}$, these two states should respond similarly to readout, independently of the reading sense. In Fig. 5(c), we show the results of in-phase and out-of-phase readouts from $\widetilde{T}$ and confirm this expectation: the results are very similar to the ones shown in Fig. 5(a) for the state T.

Thus, along the course of an out-of-phase readout of amplitude $\varepsilon_R < \varepsilon_T$, the first half cycle does not significantly change the state of the system. The contribution to the large discrepancies between the trained state T and the readout state R must therefore come from the second half-cycle. The latter involves a visit to a state of opposite maximum strain. In other words, the mechanical response of the system, and hence the memory of shear direction, is controlled by the last maximum strain.

C. Readout protocol accessing amplitude and last direction of shear

We can harness these observations to construct a readout protocol that will infer the training amplitude as well as the last direction of shear, or equivalently, detecting whether we were given for readout the state T or its antipode T'. To do so, we arbitrarily choose a direction of shear and then perform our readout as before, but this time, we also record the midcycle state M reached after applying the first half-cycle. Denoting again by R the state reached at the end of the full readout cycle, we record both the distances $d_m = d(M, T)$ and $d_{\rm st} = d(R, T)$. Figure 6 shows the readout curves for training amplitudes $\varepsilon_T = 0.02, 0.03, 0.046, 0.06, 0.064, 0.070$ and 0.074, with the readout chosen to be (a) *in-phase* or (b) *out-of-phase* relative to the sense of driving, respectively. As shown previously, when in-phase, the stroboscopic distance $d_{\rm st} = d(R, T)$ shown in Fig. 6(a) displays a clear minimum at $\varepsilon_R = \varepsilon_T$. In contrast, the midcycle distance $d_m = d(M, T)$ shows a monotonic behavior and is featureless at $\varepsilon_R = \varepsilon_T$. The simultaneous measurement of d_m and $d_{\rm st}$ thus gives access to the last direction of training in addition to the amplitude. As visible in Fig. 6(b), a similar conclusion can be drawn from the measurements performed in the case of an out-of-phase readout. As expected, this time the stroboscopic distance $d_{\rm st}$ does not permit reliable memory retrieval. However, the midcycle distance d_m remains very close to zero for readout amplitudes $\varepsilon_R \leqslant \varepsilon_T$ and then starts to rise abruptly. Moreover, this behavior persists for larger training amplitudes up to the irreversibility transition.

We therefore see that the difference of readout behavior between the full-cycle response $d(R, T)$ and the midcycle response $d(M, T)$ immediately informs us of the shear direction used for the oscillatory training. Moreover, the location of the (in-phase) minimum or the (out-of-phase) kink gives the training amplitude.

The present results were obtained with parallel readout protocols. We demonstrate in Fig. 7 that they are also easily recovered with sequential protocols. Figures 7(a) and 7(b)

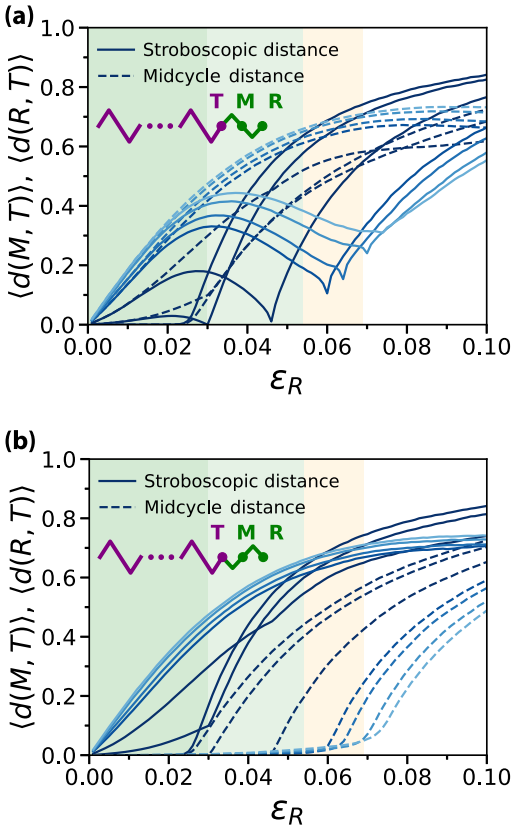

FIG. 6. Midcycle and stroboscopic readouts. Denoting by M the state reached at the end of the first half-cycle, a midcycle distance $d_m = d(M, T)$ can be defined, for the cases when the full readout cycle is in-phase or out-of-phase, panels (a) and (b), respectively. When d_m is combined with the stroboscopic distance $d_{\rm st} = d(R, T)$, their behavior reveals both the training amplitude ε_T as well as its direction.

show the responses obtained for in-phase and out-of-phase sequential readout protocols, respectively. Figure 7(c) depicts the midcycle response obtained for an out-of-phase sequential readout protocol. Here, instead of a kink separating at $\varepsilon_R = \varepsilon_T$ a region of vanishing midcycle distance from a region of large midcycle distance, we observe a smoother nonmonotonic behavior with a minimum of $d(M, T)$ at $\varepsilon_R \approx \varepsilon_T$. The nonzero values of $d(M, T)$ for $\varepsilon_R < \varepsilon_T$ here come from a simple history effect: due to the sequential nature of the readout protocol, the system is gradually modified by the series of reading cycles at $\varepsilon_{R'} \leqslant \varepsilon_R$. In contrast to the parallel readout protocol, the sequential protocol can easily be experimentally implemented, thus allowing access to both the direction and amplitude of past oscillatory training.

VI. DISCUSSION: EMERGENCE OF RETURN POINT MEMORY

We now discuss our results within the context of RPM, the property of a system to remember the values at which the direction of an external driving field is reversed [27–30,33]. One of the characteristic features of RPM is that it gives rise to nested hysteretic cycles. A typical example is shown in Fig. 8(a) where we represent a transition graph between states

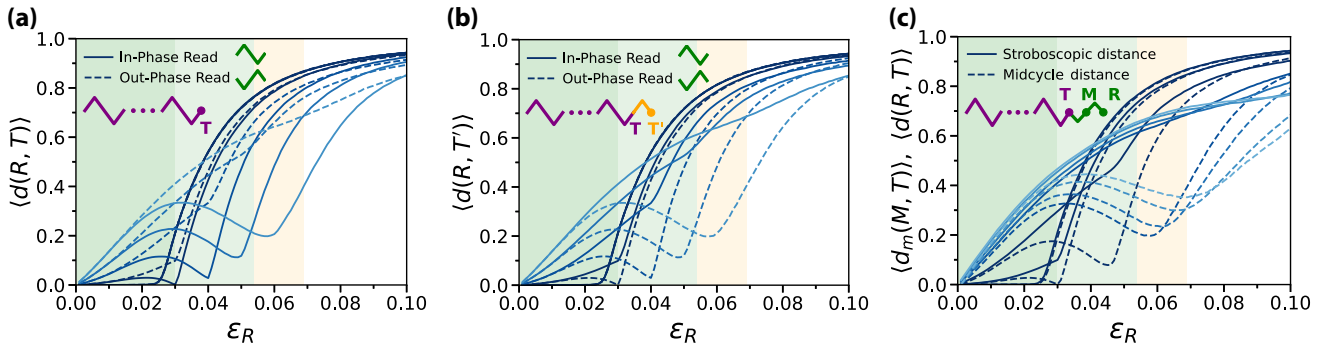

FIG. 7. Sequential readout protocols. In- and out-of-phase sequential readouts obtained from the trained states T and T', as shown in panels (a) and (b), respectively. Panel (c) shows the result of sequentially applying out-of-phase protocol with midcycle readout, i.e., the stroboscopic distance between T and R, and the distance between T and midcycle state M.

belonging to an ideal cycle obeying RPM: $0 \to \varepsilon_T \to 0 \to -\varepsilon_T \to 0$.

The sequence of transitions between configurations under increase (decrease) in strain is indicated by the black (red) dashed arrows. We keep the same notation as in the previous section to label the different states so that, as the cyclic shear protocol $0 \to \varepsilon_T \to 0 \to -\varepsilon_T \to 0$ is applied to T, the system transits through the branch configurations $T \to Y \to T' \to X \to T$.

In addition to the main cycle, we show subcycles reached by starting from T, increasing the strain to reach an intermediate state Y_1 and subsequently reducing it up to X_1 before increasing it again. Here, at Y_1 and X_1 the directions of shear are reversed, and such states are denoted as *switch-back* states. Under RPM the trajectory of such subcycles will always return to the initial switch-back state: $T \to X_2 \to T$; $Y_1 \to O_2 \to X_1 \to O_1 \to Y_1$. Note the hierarchy of nested subcycles: $Y_1 \to O_2 \to X_1 \to O_1 \to Y_1$ is included in $Y_1 \to X_1 \to X \to T \to Y_1$, which is itself included in $T \to Y \to T' \to X \to T$. Note also that, continuing from X_1 by starting to increase the strain beyond O_1, the system will eventually reach the prior switch-back state Y_1, before continuing on the pathway leading to Y and beyond [32,33]. Likewise, with T and X_2 representing a pair of consecutive switch-back states, RPM stipulates that increasing the strain at X_2 will return the system first to the previous switch-back state T. Last, note that the only exits out of the main cycle are through Y in the forward direction and X in the reverse direction of shear strain.

The graph representation helps us to illustrate the expected outcome of readout and its dependence on direction within the context of RPM. An in-phase readout of amplitude ε_T starting

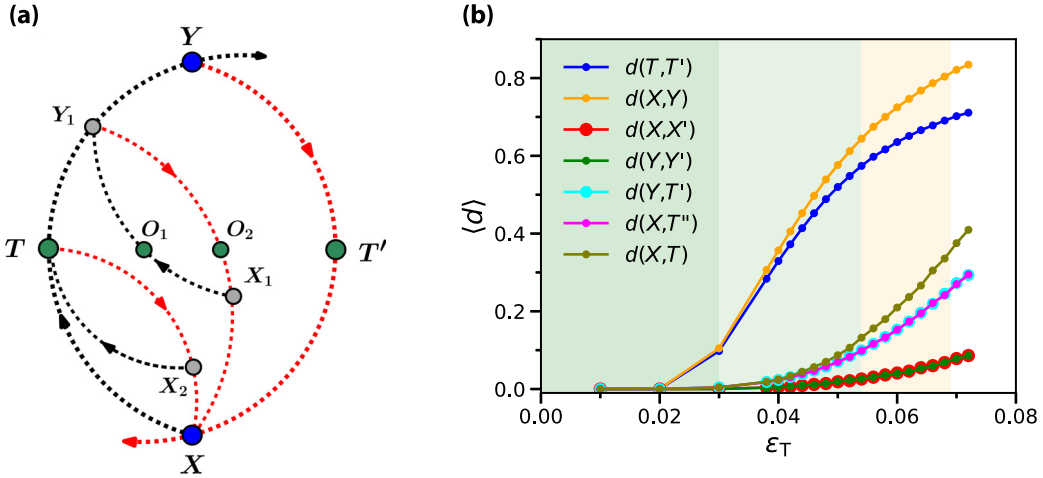

FIG. 8. Emergence of return-point memory. (a) Sketch of the transition between the branch configurations forming a monoperiodic limit-cycle in the QMEP model. When a cyclic shear protocol $0 \to \varepsilon_T \to 0 \to -\varepsilon_T \to 0$ is applied to T, the system transits through the branch configurations $T \to Y \to T' \to X \to T$, as shown. The sequence of transitions between configurations under increase (decrease) in strain is indicated by the black (red) dashed arrows. A single-cycle of *in-phase* readout $0 \to \varepsilon_R \to 0 \to -\varepsilon_R \to 0$ might follow the trajectory $T \to Y_1 \to O_2 \to X_1 \to O_1$. (b) Distances between states reachable by applying to T an in-phase quarter, half-cycle or three-quarter cycle, which are respectively labeled as Y, T', and X. A full-in phase cycle applied to T will bring the system to a state T''. Note that $T = T''$, and hence $d(T, T'') = 0$, only if the response attained at the end of the training is monoperiodic. In the case of a multiperiodic or aperiodic response, we have $T \neq T''$. The states labeled X' and Y' are reached when respectively applying to T and T' quarter phase cycles $0 \to -\varepsilon_T$ and $0 \to -\varepsilon_T$. If RPM holds, then $Y = Y'$ and $X = X'$, and the corresponding distances $d(Y, Y')$ and $d(X, X')$ would vanish.

at T simply goes through the main cycle and returns to T. We thus expect $d(R,T) = d(T,T) = 0$.

In the case of an out-of-phase readout cycle of amplitude ε_T, however, the trajectory becomes: $T \to X \to T \to Y \to T'$. Note the reversibility of the first half cycle. As mentioned in Sec. V, the application of an out-of-phase cycle sends the state T to its antipodal state T' so that we now get $d(R,T) = d(T',T) \neq 0$.

In the same spirit, a single-cycle in-phase readout $0 \to \varepsilon_R \to 0 \to -\varepsilon_R \to 0$ applied to T with amplitude $\varepsilon_R < \varepsilon_T$, might follow the trajectory $T \to Y_1 \to O_2 \to X_1 \to O_1$, so that $d(R,T) = d(O_1,T)$.

In contrast, an out-of-phase readout of the same amplitude $0 \to -\varepsilon_R \to 0 \to \varepsilon_R \to 0$ would follow the path $T \to X_2 \to T \to Y_1 \to O_2$ so that $d(R,T) = d(O_2,T)$.

The reversible paths $T \to X_2 \to T$ or $T \to X \to T$ naturally derive from the presence of the pseudogap of width $2\varepsilon_T$ observed in the distribution of backward thresholds $P(x^-)$ in Fig. 4(e) (inset). Thus, the training stage appears to lead to the development of an emergent RPM property in the range $[-2\varepsilon_T, 0]$.

As recalled in the introduction, even though the Eshelby interaction does not satisfy the no-passing rule [31], approximate RPM has already been observed both experimentally and numerically in driven amorphous solids [12,33]. Still, no-passing is only a sufficient condition to obtain RPM, not a necessary one. For instance, Deutsch *et al.* [95] could obtain exact RPM in a one-dimensional random Ising antiferromagnets when evolving from a large field (but not when starting at a small field).

A. Quantifying the distance to RPM

In this context, it is interesting to give a more quantitative characterization of the extent to which RPM holds for our mechanically annealed (trained) states T. To further probe the RPM-like behavior, we consider the states X' and Y' reached when applying to the antipodes T and T' the quarter phase cycles $0 \to -\varepsilon_T$, and $0 \to \varepsilon_T$, respectively.

Referring to Fig. 5(a), RPM would imply $X = X'$ and $Y = Y'$, so that $d(X,X') = d(Y,Y') = 0$. Figure 8(b) shows the behavior of $d(X,X')$ and $d(Y,Y')$ over a range of amplitudes ε_T. Observe that $d(X,X') \approx d(Y,Y')$ over the full range of training amplitudes shown, extending even beyond the irreversibility transition (region not shown). Moreover, the values of $d(X,X')$ and $d(Y,Y')$ remain close to zero for strain amplitudes well inside the regime of multiperiodic response (light green region), beyond which they start to increase rather slowly.

We have already noted that the distributions of plastic strengths $x^-[T]$ and its antipodal conjugate $x^+[T']$ are statistically indistinguishable and exhibit a gap for values $x^\pm < x_T$, i.e., $P(x^-[T] < x_T) \approx P(x^+[T'] < x_T) \approx 0$. This suggests that a strain increase (decrease) by ε_T at X (Y) will result in a predominantly elastic response.

Denote the sequence of states visited when a single in-phase shear strain cycle of amplitude ε_T is applied to T by $T \to Y \to T' \to X \to T''$, where $T = T''$ if the response is monoperiodic. The purple and cyan curves in Fig. 8(b) show how $d(X,T'')$ and $d(Y,T')$ change with ε_T. First, we see again that their behavior is statistically indistinguishable, as expected by the parity of antipodal states. Moreover, for the monoperiodic regime of training amplitudes (darker green region), these values remain close to zero and start to increase in the multiperiodic regime, implying that the transitions $X \to T''$ and $Y \to T'$ on the limit-cycle are nearly elastic for sufficiently low training amplitudes.

B. Preisach-like model of directional memory

In a complementary perspective of probing the emergent RPM behavior of the QMEP model, we now compare our simulation results with predictions of a simple Preisach-like model, which is a minimal model exhibiting RPM and and thus directional memory. The full details of this minimal model of directional memory (hypotheses and derivations of the analytical predictions) are presented in the Appendix B.

Specifically, assuming the elastic character of the transitions $X \leftrightarrow T$ and $Y \leftrightarrow T'$ allows us to formulate a prediction of the in-and out-of-phase stroboscopic readout distances, $d_{\rm st}^{\rm in}$ and $d_{\rm st}^{\rm out}$, cf. (1). Note that our prediction will be based entirely on the forward plastic strength $x^+[T]$. In other words, we build our model only on the knowledge of the trained state T obtained after mechanical annealing.

As detailed in the Appendix B, the predictions for the out-of-phase readout is given by

$$d_{\rm st}^{\rm out}(R,T) = \text{Prob}(x_{ij}^+[T] \leqslant x_R), \tag{2}$$

while for the in-phase readout we get

$$d_{\rm st}^{\rm in} = \begin{cases} \text{Prob}(x_{ij}^+[T] \leqslant x_R)\,\text{Prob}(x_R < x_{ij}^+[T] \leqslant x_T \,|\, x_{ij}^+[T] \leqslant x_T), & \varepsilon_R \leqslant \varepsilon_T, \\ \text{Prob}(x_T < x_{ij}^+[T] \leqslant x_R), & \varepsilon_R > \varepsilon_T. \end{cases} \tag{3}$$

For the case of out-of-phase readouts, Fig. 9(a) shows a comparison of the prediction of Eq. (2), using the numerically obtained distributions of $x_{ij}^+[T]$ shown in Fig. 4(e) (inset), with the readout results obtained from numerical simulations for training amplitudes $\varepsilon_T = 0.028, 0.03, 0.038, 0.044, 0.054$, and 0.064. The predictions of the lowest three training amplitudes agree rather well over a range $\varepsilon_R \lesssim \varepsilon_T$. For $\varepsilon_R > \varepsilon_T$, these predictions deviate significantly for the lowest two training amplitudes. At higher training amplitudes, a good agreement with the prediction is reached only for low values of readout.

For the case of in-phase readouts, Fig. 9(b) compares the in-phase readout distances $d_{\rm st}^{\rm in}$ from our simulations with the prediction obtained from Eq. (3). The results for training amplitudes are shown below $\varepsilon_T = 0.028, 0.03, 0.038, 0.044$, and 0.05 (from bottom to top and in increasingly lighter

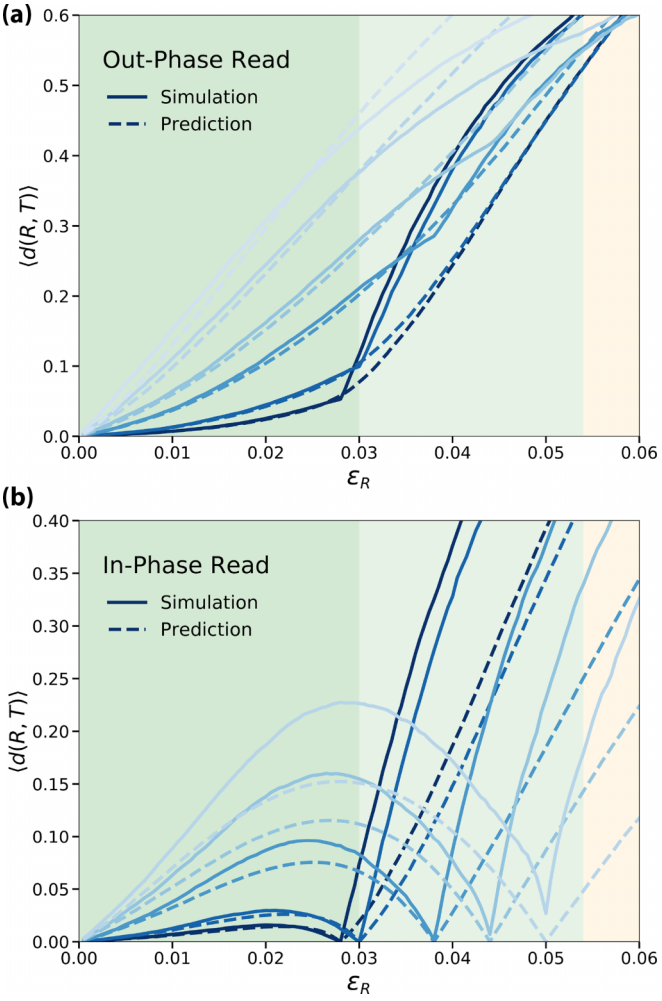

FIG. 9. Simulation and theoretical predictions for the in- and out-of-phase readout distances. (a) Comparison of the out-of-phase readout response obtained from simulations (solid lines) with the theoretical prediction (dashed lines) based on the density of local sites susceptible to yielding Eq. (2). The training amplitudes considered are $\varepsilon_T = 0.028, 0.03, 0.038, 0.044, 0.054$ and 0.064 (from bottom to top). (b) The in-phase readout from simulations compared to theoretical predictions for training amplitudes $\varepsilon_T = 0.028, 0.03, 0.038, 0.044$, and 0.05 (bottom to top).

shades of blue). Considering first the readout regimes where $\varepsilon_R \leqslant \varepsilon_T$, we see that the agreement with the predicted result is rather good for training amplitudes ε_T in the region where the cyclic response is monoperiodic (region shaded in darker green). For all training amplitudes shown, the predicted asymmetric shape of $d_{\rm st}^{\rm in}$ matches well the numerical results. However, with increasing training amplitudes, the theoretical results systematically underestimate the readout distances. Finally, in the region $\varepsilon_R > \varepsilon_T$, the sharp rise in $d_{\rm st}^{\rm in}$ is captured well by our predictions but the discrepancies increase with ε_T.

To summarize, positing that the cyclic shearing has led to a periodic response and ignoring elastic interactions amounts to casting the *future* response of the amorphous solid as that of a Preisach model, whose thresholds have been drawn from the distributions of $x^+[T]$ and $x^-[T']$. As the Preisach model exhibits RPM, the extent to which the Preisach approximation captures the actual readout behavior can be regarded as a probe of RPM. Let us stress that this Preisach reduction is emergent, as it takes the distribution of trained thresholds $x^+[T]$ as given.

VII. CONCLUSION

The study of our QMEP model of amorphous solids has allowed us to reproduce and understand the memory behavior that has been observed both experimentally in dense suspensions and numerically in particle simulations. We have provided a detailed description of the mechanical processes underlying memory formation. Mechanical annealing leads to the self-organization of local plasticity via the evolution of stress thresholds. We observe in particular the development of a clear forward-backward anisotropy in the local yield stresses. This emergent self-organization in turn encodes features of the driving history.

We developed experimentally testable readout protocols from which, besides the training amplitude, the direction of the last shear can be recovered as well. The evolution of the readout response upon increasing training amplitude shows that the memory amplitude and direction gradually degrades due to the appearance of multiperiodic limit cycles and the gradual loss of plastic reversibility. Nevertheless, this memory behavior persists even past the irreversibility transition. Interestingly, the behavior of sample-to-sample fluctuations of the readout response with training amplitude provides a direct means to identify the irreversibility transition.

The QMEP model, while being a minimal mesoscale model of an amorphous solid, has allowed us to understand in detail the mechanical mechanisms that lead to memory formation under cyclic shear. It has provided direct access to structural mechanical information, such as the fields of local stresses, stress thresholds and plastic strengths, which in turn allowed us to link memory formation with mechanical annealing.

These findings naturally motivate more detailed studies on the spatial support underlying the observed mechanical memory. For example, it was recently found that the phenomenon of memory formation as evidenced by the in- and out-of-phase readout curves emerges even in the case where instead of applying cyclical shear at training amplitude ε_T, the applied strain follows a random walk which is confined to a strain interval $\pm\varepsilon_T$ [96].

A key feature of the QMEP model is the quenched character of the disorder: Each local cell lives in a well-defined frozen random landscape so that it may revisit the very same series of plastic thresholds upon forward and reverse shear. This strong assumption naturally motivates a more detailed characterization of the local mechanical disorder in atomistic simulations of glassy materials [60,61]. Nevertheless, the quenched character of the stress landscape does not impede the development of a driving-induced selection process and the emergence of self-organization.

Our results of encoding and subsequent readout of the memory and direction of training amplitude reveal behavior that is qualitatively consistent with what one would expect

from systems that obey RPM. Building on this observation, we developed a simple Preisach-like model of directional memory, which qualitatively reproduces both the in-phase and the out-of-phase readout responses. Note again that this quasi-RPM behavior, observed in experiments and numerical simulations [12,33], is somewhat unexpected and deserves more scrutiny.

Our findings suggest that RPM-like behavior *emerges* as a result of mechanical annealing. In particular, the prediction Eq. (2) of our Preisach-like model for the out-of-phase readout $d_{\rm st}^{\rm out}$ suggests that we can interpret $d_{\rm st}^{\rm out}$ as the fraction of sites that can yield under a given readout amplitude. Seen this way, the change of slope in the empirical readout distance $d_{\rm st}^{\rm out}$ around $\varepsilon_R \approx \varepsilon_T$ is due to the readout causing the excitation of hitherto mechanically inaccessible (untrained) degrees of freedom. The behavior of the midcycle distances with training amplitudes, shown in Fig. 5(e), further supports this interpretation. We plan to pursue these ideas in future work. Another perspective of interest would consist of exploring further the connection between Preisach models and mean field models of amorphous plasticity accounting for structural disorder [78–80].

In summary, the mesoscale model of an amorphous solid subject to mechanical annealing by cyclic shear has provided detailed insights into the mechanical processes underlying memory formation. We find that the driving leads to the self-organization of local plasticity, which, via the evolution of stress thresholds under mechanical annealing, leads to the encoding of features of the driving history.

Last, the self-organization of driven disordered systems under mechanical annealing bears similarities to evolutionary processes of mutation and selection in changing environments [97–100]. Pursuing this analogy in the context of annealing a sheared amorphous solid, we can think of plastic events as mutations, while annealing by cyclic shear furnishes a selection process where plastic events are created and discarded under driving. The self-organization under annealing is a search for a collection of persistent plastic events that can be repeatedly triggered in full or in subsets as the driving cycle or its subcycles are traversed, thus giving rise to mechanical reversibility and memory [34,81]. As noted above, this type of self-organization can occur even when instead of cyclically shearing the system is driven by a randomly varying external strain, which mimics a system interacting with a fluctuating environment [96].

However, the evolution of organisms is governed by a fitness landscape which is a proxy for the ability of genotypes to grow in a given environment, with evolution selecting for higher fitness [101–103]. In the case of the sheared amorphous solid, the physical property corresponding to fitness is the gain in elasticity, and hence the loss of plasticity that is the result of the hardening under cyclic annealing. This in turn implies that the response to cyclic shear involves increasingly fewer plastic events, and hence a gradual reduction of energy dissipated by these during a driving cycle. More generally, the *in silico* evolution of the amorphous solid is that of its underlying disorder. The mesoscale model considered here constitutes a minimal model with a dynamic disorder landscape whose evolution can be compared with that of fitness landscapes.

ACKNOWLEDGMENTS

The research of M.M. was funded by the Deutsche Forschungsgemeinschaft (DFG, German Research Foundation) under Project No. 398962893 and CRC 1310 *Predictability in Evolution*. M.M. thanks PMMH and ESPCI for their kind hospitality during multiple stays, which were made possible by grants from Chaire Joliot. This project has received funding from the European Union's Horizon 2020 research and innovation programme under the Marie Skłodowska-Curie Grant Agreement No. 754387. D.V. acknowledges insightful discussions with Craig Maloney and Elisabeth Agoritsas.

DATA AVAILABILITY

The data that support the finding of this article are available from the authors upon reasonable request.

APPENDIX A: BASICS OF THE QMEP MODEL

We consider a $N \times N$ lattice Λ of mesoscale cells indexed as (i, j). The stress and strain fields are denoted by ε_{ij} and σ_{ij}, respectively. The global stress Σ and the global strain ε are the spatial averages of these microscopic fields: $\Sigma = \sum_{ij} \sigma_{ij}/N^2$, $\varepsilon = \sum_{ij} \varepsilon_{ij}/N^2$. The local strain is decomposed into an elastic strain and a plastic strain $\varepsilon_{ij} = \varepsilon_{ij}^{\rm el} + \varepsilon_{ij}^{\rm pl}$ where $\varepsilon_{ij}^{\rm el} = \sigma_{ij}/2\mu$ (with μ the shear modulus) and $\varepsilon_{ij}^{\rm pl}$ is the residual strain one would obtain for a null local stress $\sigma_{ij} = 0$.

As discussed in Sec. II A and illustrated in Fig. 1, we consider a quenched random distribution of plastic thresholds: for each cell (i, j), we assign a pair $(\sigma_{ij}^-, \sigma_{ij}^+)$ of plastic thresholds that bound the mechanical stability range of the cell and constitute a *local elastic branch*. Whenever a cell (i^*, j^*) gets unstable, say in the positive direction, i.e., $\sigma_{i^*j^*} \geqslant \sigma_{i^*j^*}^+$, it leaves the elastic branch ℓ and lands on a new elastic branch $\ell + 1$ bounded by two *new* plastic thresholds $\sigma_{i^*j^*}^-, \sigma_{i^*j^*}^+$ and the local plastic strain $\varepsilon_{i^*j^*}^{\rm pl}$ is incremented by a small amount $\Delta\epsilon$.

This local plastic event at cell (i^*, j^*) induces a global stress drop, $\Sigma \to \Sigma - 2\Delta\varepsilon/N^2$ and a stress redistribution, $\sigma_{ij} \to \sigma_{ij} + \Delta\varepsilon \cdot G_{i-i^*,j-j^*}$, where G is the discrete implementation of the Eshelby kernel, i.e., the elastic response of an elastic matrix to a unit shear plastic shear strain in one cell [53,71]. In real space we have the far field $G_{mn} \propto \cos 4\theta_{mn}/r_{mn}^2$ with (r_{mn}, θ_{mn}) the polar coordinates of cell (m, n). The interplay between the disorder and this quadrupolar (non convex) Eshelby kernel is at the origin of the complex phenomenology of amorphous plasticity.

APPENDIX B: PREISACH-LIKE MODEL OF DIRECTIONAL MEMORY

We consider first the case of an out-of-phase readout, $0 \to -\varepsilon_R \to 0 \to \varepsilon_R \to 0$ and let $x_R = 2\varepsilon_R$. By assumption, the first half of the readout cycle is perfectly elastic and hence returns the system to T. In the second half of the cycle, all sites (i, j) for which $x_{ij}^+[T] \leqslant x_R$, are candidates to yield during the strain increase $0 \to \varepsilon_R$. Due to avalanches during this

half-cycle, some additional sites may be destabilized, while owing to the quadrupolar nature of stress redistribution, some of the initial candidate sites may be stabilized by the yielded sites. We will ignore these two types of sites and assume that the sites (i, j) that yielded during the strain increase are precisely those for which $x_{ij}^{+}[T] \leqslant x_R$. In addition, we will assume that the response to the final strain reduction $\varepsilon_R \to 0$ is purely elastic. Recalling that $d_{\rm st}^{\rm out}$ is the fraction of sites that did not return to their local branch at the end of the readout cycle, this leads to the prediction that

$$d_{\rm st}^{\rm out} = \text{Prob}(x_{ij}^{+}[T] \leqslant x_R). \tag{B1}$$

A similar approach can be applied to obtain a prediction for the in-phase readouts and leads for $\varepsilon_R \leqslant \varepsilon_T$ to

$$d_{\rm st}^{\rm in} = \text{Prob}(x_{ij}^{+}[T] \leqslant x_R) \times \text{Prob}(x_R < x_{ij}^{+}[T] \leqslant x_T \,|\, x_{ij}^{+}[T] \leqslant x_T), \tag{B2}$$

while in the case that $\varepsilon_R > \varepsilon_T$, we have

$$d_{\rm st}^{\rm in} = \text{Prob}(x_T < x_{ij}^{+}[T] \leqslant x_R). \tag{B3}$$

This result for the in-phase readout follows from a set of assumptions that we state next. Denoting by F_T and F_R the set of sites (i, j) such that $x_{ij}^{+}[T] \leqslant x_T$ and $x_{ij}^{+}[T] \leqslant x_R$, respectively, we consider a sequence of configurations visited upon a readout cycle whose transition pathway is $T \to Y_1 \to O_2 \to X_1 \to O_1$, as sketched in Fig. 8(a) We then assume that

(i) the response after training is cyclic and monoperiodic,

(ii) the responses in the segments $Y_1 \to O_2$ and $X_1 \to O_1$ are purely elastic,

(iii) the set of sites that yield during the pathways $T \to Y_1$ is given by F_R.

Denoting by F_R^{-} the set of sites that yield during the pathway $O_2 \to X_1$, i.e.,

$$F_R^{-} = \{(i, j) : x_{ij}^{-}[O_2] \leqslant x_R\}, \tag{B4}$$

the above assumptions imply that $|F_R^{-}| = |F_R|$ and

$$d_{\rm st}^{\rm in} = \frac{|F_R \triangle F_R^{-}|}{|\Lambda|}, \tag{B5}$$

where $A \triangle B$ is the symmetric set difference corresponding to the set of elements that are in A but not in B, or in B but not in A.

To estimate $d_{\rm st}^{\rm in}$, we make the following two additional assumptions:

(iv)

$$F_R^{-} \subset F_T, \quad \varepsilon_R \leqslant \varepsilon_T, \qquad F_T \subset F_R^{-}, \quad \varepsilon_R > \varepsilon_T, \tag{B6}$$

(v) in the case that $\varepsilon_R \leqslant \varepsilon_T$, the set F_R^{-} is obtained by assigning to each site $(i, j) \in F_T$ a plastic strength value $x_{ij}^{-}[O_2]$ that is drawn independently and identically (iid) from the distribution of $x_{ij}^{+}[T]$ conditioned on $x_{ij}^{+}[T] \leqslant x_T$. For $\varepsilon_R > \varepsilon_T$, $|F_T|$ sites are drawn iid as in the previous case, while the remaining sites are drawn iid, but conditioned on $x_T < x_{ij}^{+}[T] \leqslant x_R$.

Using assumption (v) to replace the right-hand side of Eq. (B5) by its average value then leads to Eqs. (B2) and (B3). Let us note that when $\varepsilon_R = \varepsilon_T$, our assumptions imply that $F_T = F_R = F_R^{-}$, so that from Eq. (B5) it follows that $d_{\rm st}^{\rm in} = 0$.

Note that the choice of distribution described in assumption (v) is motivated by our empirical observation of polarity, which implies that the distributions of plastic strengths $x^{+}[T]$ and $x^{-}[T']$ are identical. Hence, all that assumption (v) does is to replace the distribution of $x^{-}[O_2]$ with that of $x^{-}[T']$, which by the polarity assumption has the same distribution as $x^{+}[T]$.

Assumptions (iv) and (v) effectively impose RPM by turning the theoretical description into a Preisach model [27,39]. Here, each site $(i, j) \in F_T$ emulates a Preisach hysteron, i.e., a hysteresis unit that can hysteretically switch between two states. In the QMEP model, these hysterons emerge under training and correspond to the local elastic branches ℓ_{ij} at T and T', along with their switching fields which are determined by $x_{ij}^{+}[T]$ and $x_{ij}^{-}[T']$. This description ignores interactions between sites that arise when a given site yields, triggering a redistribution of elastic stresses that will lead to an update of plastic strengths $x^{\pm}$ at all sites. With larger training and readout amplitudes, such interactions will become increasingly dominant, invalidating the assumptions underlying our description.

[1] N. C. Keim, J. D. Paulsen, Z. Zeravcic, S. Sastry, and S. R. Nagel, Rev. Mod. Phys. **91**, 035002 (2019).

[2] J. D. Paulsen and N. C. Keim, Annu. Rev. Condens. Matter Phys. **16**, 61 (2025).

[3] D. Shohat, D. Hexner, and Y. Lahini, Proc. Natl. Acad. Sci. USA **119**, e2200028119 (2022).

[4] H. A. Vinutha, M. Marchand, M. Caggioni, V. V. Vasisht, E. Del Gado, and V. Trappe, PNAS Nexus **3**, 441 (2024).

[5] P. Edera, M. Bantawa, S. Aime, R. T. Bonnecaze, and M. Cloitre, Phys. Rev. X **15**, 011043 (2025).

[6] D. J. Pine, J. P. Gollub, J. Brady, and A. M. Leshansky, Nature (London) **438**, 997 (2005).

[7] L. Corte, P. M. Chaikin, J. P. Gollub, and D. J. Pine, Nat. Phys. **4**, 420 (2008).

[8] N. C. Keim and P. E. Arratia, Soft Matter **9**, 6222 (2013).

[9] N. C. Keim and P. E. Arratia, Phys. Rev. Lett. **112**, 028302 (2014).

[10] J. D. Paulsen, N. C. Keim, and S. R. Nagel, Phys. Rev. Lett. **113**, 068301 (2014).

[11] S. Mukherji, N. Kandula, A. K. Sood, and R. Ganapathy, Phys. Rev. Lett. **122**, 158001 (2019).

[12] N. C. Keim, J. Hass, B. Kroger, and D. Wieker, Phys. Rev. Res. **2**, 012004(R) (2020).

[13] I. Regev, T. Lookman, and C. Reichhardt, Phys. Rev. E **88**, 062401 (2013).

[14] D. Fiocco, G. Foffi, and S. Sastry, Phys. Rev. E **88**, 020301(R) (2013).

[15] N. V. Priezjev, Phys. Rev. E **93**, 013001 (2016).

[16] T. Kawasaki and L. Berthier, Phys. Rev. E **94**, 022615 (2016).
[17] C. Reichhardt, I. Regev, K. Dahmen, S. Okuma, and C. J. O. Reichhardt, Phys. Rev. Res. **5**, 021001 (2023).
[18] N. C. Keim and S. R. Nagel, Phys. Rev. Lett. **107**, 010603 (2011).
[19] D. Fiocco, G. Foffi, and S. Sastry, Phys. Rev. Lett. **112**, 025702 (2014).
[20] M. Adhikari and S. Sastry, Eur. Phys. J. E **41**, 105 (2018).
[21] I. Regev, I. Attia, K. Dahmen, S. Sastry, and M. Mungan, Phys. Rev. E **103**, 062614 (2021).
[22] Z. A. Benson, A. Peshkov, D. C. Richardson, and W. Losert, Phys. Rev. E **103**, 062906 (2021).
[23] F. Arceri, E. I. Corwin, and V. F. Hagh, Phys. Rev. E **104**, 044907 (2021).
[24] B. Flavio di Dio, F. Khabaz, R. T. Bonnecaze, and M. Cloitre, J. Rheol. **66**, 717 (2022).
[25] N. C. Keim and D. Medina, Sci. Adv. **8**, eabo1614 (2022).
[26] D. Shohat and Y. Lahini, Phys. Rev. Lett. **130**, 048202 (2023).
[27] F. Preisach, Z. Phys. **94**, 277 (1935).
[28] D. H. Everett and W. I. Whitton, Trans. Faraday Soc. **50**, 1077 (1954).
[29] J. A. Barker, D. Schreiber, B. Huth, and D. H. Everett, Proc. Roy. Soc. London. A. Math. Phys. Sci. **386**, 251 (1983).
[30] J. P. Sethna, K. Dahmen, S. Kartha, J. A. Krumhansl, B. W. Roberts, and J. D. Shore, Phys. Rev. Lett. **70**, 3347 (1993).
[31] A. A. Middleton, Phys. Rev. Lett. **68**, 670 (1992).
[32] M. Mungan and M. M. Terzi, Ann. Henri Poincaré **20**, 2819 (2019).
[33] M. Mungan, S. Sastry, K. Dahmen, and I. Regev, Phys. Rev. Lett. **123**, 178002 (2019).
[34] M. Mungan, Proc. Natl. Acad. Sci. USA **119**, e2208743119 (2022).
[35] M. L. Falk and J. S. Langer, Phys. Rev. E **57**, 7192 (1998).
[36] A. Barbot, M. Lerbinger, A. Hernandez-Garcia, R. García-García, M. L. Falk, D. Vandembroucq, and S. Patinet, Phys. Rev. E **97**, 033001 (2018).
[37] G. Bertotti and I. D. Mayergoyz, *The Science of Hysteresis: Hysteresis in Materials* (Gulf Professional Publishing, Houston, TX, 2006), Vol. 3.
[38] M. Brokate and J. Sprekels, *Hysteresis and Phase Transitions* (Springer Science & Business Media, Berlin, 2012), Vol. 121.
[39] M. M. Terzi and M. Mungan, Phys. Rev. E **102**, 012122 (2020).
[40] H. Bense and M. van Hecke, Proc. Natl. Acad. Sci. USA **118**, e2111436118 (2021).
[41] N. C. Keim and J. D. Paulsen, Sci. Adv. **7**, eabg7685 (2021).
[42] C. W. Lindeman and S. R. Nagel, Sci. Adv. **7**, eabg7133 (2021).
[43] M. van Hecke, Phys. Rev. E **104**, 054608 (2021).
[44] A. Szulc, M. Mungan, and I. Regev, J. Chem. Phys. **156**, 164506 (2022).
[45] G. Muhaxheri and C. D. Santangelo, Phys. Rev. E **110**, 024209 (2024).
[46] C. W. Lindeman, T. R. Jalowiec, and N. C. Keim, Sci. Adv. **11**, eadr5933 (2025).
[47] J. Liu, M. Teunisse, G. Korovin, I. R. Vermaire, L. Jin, H. Bense, and M. van Hecke, Proc. Natl. Acad. Sci. USA **121**, e2308414121 (2024).
[48] C. Sirote-Katz, D. Shohat, C. Merrigan, Y. Lahini, C. Nisoli, and Y. Shokef, Nat. Commun. **15**, 4008 (2024).
[49] I. Regev, J. Weber, C. Reichhardt, K. A. Dahmen, and T. Lookman, Nat. Commun. **6**, 8805 (2015).
[50] W.-T. Yeh, M. Ozawa, K. Miyazaki, T. Kawasaki, and L. Berthier, Phys. Rev. Lett. **124**, 225502 (2020).
[51] H. Bhaumik, G. Foffi, and S. Sastry, Proc. Natl. Acad. Sci. USA **118**, e2100227118 (2021).
[52] A. Nicolas, E. E. Ferrero, K. Martens, and J.-L. Barrat, Rev. Mod. Phys. **90**, 045006 (2018).
[53] J. D. Eshelby, Proc. R. Soc. London A **241**, 376 (1957).
[54] G. Picard, A. Ajdari, L. Bocquet, and F. Lequeux, Eur. Phys. J. E **15**, 371 (2004).
[55] B. Tyukodi, D. Vandembroucq, and C. E. Maloney, Phys. Rev. Lett. **121**, 145501 (2018).
[56] J. Lin, E. Lerner, A. Rosso, and M. Wyart, Proc. Natl. Acad. Sci. USA **111**, 14382 (2014).
[57] D. Vandembroucq and S. Roux, Phys. Rev. B **84**, 134210 (2011).
[58] D. F. Castellanos and M. Zaiser, Phys. Rev. Lett. **121**, 125501 (2018).
[59] F. Puosi, J. Olivier, and K. Martens, Soft Matter **11**, 7639 (2015).
[60] S. Patinet, D. Vandembroucq, and M. L. Falk, Phys. Rev. Lett. **117**, 045501 (2016).
[61] D. Richard, M. Ozawa, S. Patinet, E. Stanifer, B. Shang, S. A. Ridout, B. Xu, G. Zhang, P. K. Morse, J. L. Barrat, L. Berthier, M. L. Falk, P. Guan, A. J. Liu, K. Martens, S. Sastry, D. Vandembroucq, E. Lerner, and M. L. Manning, Phys. Rev. Mater. **4**, 113609 (2020).
[62] D. Ruan, S. Patinet, and M. L. Falk, J. Mech. Phys. Solids **158**, 104671 (2022).
[63] D. F. Castellanos, S. Roux, and S. Patinet, Comptes Rendus Phys. **22**, 135 (2021).
[64] C. Liu, S. Dutta, P. Chaudhuri, and K. Martens, Phys. Rev. Lett. **126**, 138005 (2021).
[65] D. F. Castellanos, S. Roux, and S. Patinet, Acta Mater. **241**, 118405 (2022).
[66] B. Tyukodi, A. Barbot, R. García-García, M. Lerbinger, S. Patinet, and D. Vandembroucq, Comptes Rendus Phys. **24**, 113 (2023).
[67] K. Khirallah, B. Tyukodi, D. Vandembroucq, and C. E. Maloney, Phys. Rev. Lett. **126**, 218005 (2021).
[68] C. Liu, E. E. Ferrero, E. A. Jagla, K. Martens, A. Rosso, and L. Talon, J. Chem. Phys. **156**, 104902 (2022).
[69] D. Kumar, S. Patinet, C. E. Maloney, I. Regev, D. Vandembroucq, and M. Mungan, J. Chem. Phys. **157**, 174504 (2022).
[70] J.-C. Baret, D. Vandembroucq, and S. Roux, Phys. Rev. Lett. **89**, 195506 (2002).
[71] B. Tyukodi, S. Patinet, S. Roux, and D. Vandembroucq, Phys. Rev. E **93**, 063005 (2016).
[72] T. Jocteur, S. Figueiredo, K. Martens, E. Bertin, and R. Mari, Phys. Rev. Lett. **132**, 268203 (2024).
[73] V. V. Bulatov and A. S. Argon, Modell. Simul. Mater. Sci. Eng. **2**, 167 (1994).
[74] G. Picard, A. Ajdari, L. Bocquet, and F. Lequeux, Phys. Rev. E **66**, 051501 (2002).
[75] P. Hébraud and F. Lequeux, Phys. Rev. Lett. **81**, 2934 (1998).

[76] P. Sollich, F. Lequeux, P. Hébraud, and M. E. Cates, Phys. Rev. Lett. **78**, 2020 (1997).
[77] P. Sollich, Phys. Rev. E **58**, 738 (1998).
[78] E. Agoritsas, E. Bertin, K. Martens, and J.-L. Barrat, Eur. Phys. J. E **38**, 71 (2015).
[79] E. Agoritsas and K. Martens, Soft Matter **13**, 4653 (2017).
[80] J. T. Parley, S. Sastry, and P. Sollich, Phys. Rev. Lett. **128**, 198001 (2022).
[81] D. Kumar, Memory effects and yielding in a mesoscale model of amorphous plasticity, Ph.D. thesis, Université Paris Sciences et Lettres, Paris, 2023.
[82] M. Lundberg, K. Krishan, N. Xu, C. S. O'Hern, and M. Dennin, Phys. Rev. E **77**, 041505 (2008).
[83] C. E. Maloney and A. Lemaître, Phys. Rev. E **74**, 016118 (2006).
[84] A. Elgailani, D. Vandembroucq, and C. E. Maloney, Phys. Rev. Lett. **134**, 148204 (2025).
[85] J. M. Deutsch and O. Narayan, Phys. Rev. Lett. **91**, 200601 (2003).
[86] M. O. Lavrentovich, A. J. Liu, and S. R. Nagel, Phys. Rev. E **96**, 020101(R) (2017).
[87] F. Radjai and S. Roux, Contact dynamics study of 2D granular media: Critical states and relevant internal variables, *The Physics of Granular Media* (Wiley, Berlin, 2004), pp. 165–186.
[88] C. L. Rountree, D. Vandembroucq, M. Talamali, E. Bouchaud, and S. Roux, Phys. Rev. Lett. **102**, 195501 (2009).
[89] T. Sato, N. Funamori, and T. Yagi, J. Appl. Phys. **114**, 103509 (2013).
[90] D. Wakabayashi, N. Funamori, and T. Sato, Phys. Rev. B **91**, 014106 (2015).
[91] S. Patinet, A. Barbot, M. Lerbinger, D. Vandembroucq, and A. Lemaître, Phys. Rev. Lett. **124**, 205503 (2020).
[92] A. D. S. Parmar, S. Kumar, and S. Sastry, Phys. Rev. X **9**, 021018 (2019).
[93] S. Sastry, Phys. Rev. Lett. **126**, 255501 (2021).
[94] M. Mungan and S. Sastry, Phys. Rev. Lett. **127**, 248002 (2021).
[95] J. M. Deutsch, A. Dhar, and O. Narayan, Phys. Rev. Lett. **92**, 227203 (2004).
[96] M. Mungan, D. Kumar, S. Patinet, and D. Vandembroucq, Phys. Rev. Lett. **134**, 178203 (2025).
[97] P. Bak and K. Sneppen, Phys. Rev. Lett. **71**, 4083 (1993).
[98] S. G. Das, J. Krug, and M. Mungan, Phys. Rev. X **12**, 031040 (2022).
[99] S. G. Das, M. Mungan, and J. Krug, Proc. Natl. Acad. Sci. USA **122**, e2422520122 (2025).
[100] H. Jaeger, A. Murugan, and S. Nagel, Soft Matter **20**, 6695 (2024).
[101] S. Wright, in *Proceedings of the 6th International Congress of Genetics* (Brooklyn Botanic Garden, Brooklyn, NY, 1932), Vol. 1, pp. 356–366.
[102] S. Wright, Annu. Rev. Genet. **16**, 1 (1982).
[103] D. M. Weinreich, R. A. Watson, and L. Chao, Evolution **59**, 1165 (2005).